Redshift evolution of galaxy group X-ray properties in the SIMBA simulations

Dylan Robson[1]⋆ and Romeel Davé [1,2,3]⋆

[1]*Institute for Astronomy, University of Edinburgh, Edinburgh, EH9 3HJ, UK*
[2]*University of the Western Cape, Bellville, Cape Town 7535, South Africa*
[3]*South African Astronomical Observatories, Observatory, Cape Town 7925, South Africa*

ABSTRACT

We examine the evolution of intragroup gas rest-frame X-ray scaling relations for group-sized haloes ($M_{500} = 10^{12.3}$–10^{15} $M_\odot$) in the SIMBA galaxy formation simulation. X-ray luminosity L_X versus M_{500} shows increasing deviation from self-similarity from $z = 3 \rightarrow 0$, with $M_{500} < 10^{13.5}$ $M_\odot$ haloes exhibiting a large reduction in L_X and slight increase in X-ray luminosity-weighted temperature T_X. These shifts are driven by a strong drop in f_{gas} with time for these haloes, and coincides with the onset of SIMBA's black hole (BH) jet feedback, occurring when $M_{BH} > 10^{7.5}$ $M_\odot$ and Eddington ratio <0.2, in group haloes at $z \sim 1.5$. The connection with BH feedback is corroborated by $f_{BH} \equiv M_{BH}/M_{500}$ in $M_{500} < 10^{13.5}$ $M_\odot$ haloes being strongly anticorrelated with L_X and f_{gas} at $z \lesssim 1.5$. This is further reflected in the scatter of $L_X - T_X$: haloes with small f_{BH} lie near self-similarity, while those with the highest f_{BH} lie furthest below. Turning off jet feedback results in mostly self-similar behaviour down to $z = 0$. For the X-ray weighted metallicity Z_X, stellar feedback impacts the enrichment of halo gas. Finally, halo profiles show that jet feedback flattens the electron density and entropy profiles, and introduces a core in X-ray surface brightness, particularly at $M_{500} < 10^{13.5}$ $M_\odot$. This argues that in SIMBA, intragroup X-ray evolution is largely driven by jet feedback removing hot gas from the cores of massive groups, and expelling gas altogether in less massive groups.

Key words: galaxies: evolution – galaxies: formation – galaxies: groups: general – X-rays: galaxies: clusters.

1 INTRODUCTION

Clusters of galaxies are formed as peaks in the primordial density field collapse and subsequently grow through hierarchical clustering. As probes of the high-mass tail of the spectrum of mass perturbations, these clusters allow us to constrain the evolution of structure in the universe. The basic properties of these clusters are largely determined by initial conditions and the dynamically dominant dissipationless dark matter, although baryonic processes can have a non-trivial impact particularly in the group regime. Models of dark matter-driven dissipationless collapse are none the less broadly successful in predicting relationships between cluster properties, the most common of which being the self-similar model of clusters (Kaiser 1986). In this scenario, groups and clusters are identical when scaled by mass, which is known as strong self-similarity (Bower 1997). Under strong self-similarity, the slope of the resulting scaling relations is not expected to evolve with redshift, although there is an expected evolution in the normalization due to the changing density of the Universe. This model provides us with a clear baseline from which to examine the impact of baryonic physics in cluster formation.

As matter collapses to form these clusters gas experiences adiabatic compression and shock heating, creating a hot intracluster medium (ICM) with temperatures $T > 10^6$ K, which emit X-rays as a result of thermal bremsstrahlung as well as metal emission

lines. This hot gas cools and settles into hydrostatic equilibrium. Radiative cooling from dense gas in the cores of all but the most massive systems is expected to create a cooling flow that feeds star formation and accretion on to the central supermassive black hole (BH). However, observed star formation rates (SFRs) are orders of magnitude lower than cooling flow estimates would suggest (Fabian 2002), resulting in the cluster cooling flow problem.

Feedback from active galactic nuclei (AGNs) is often proposed as the solution to the cooling flow problem (Bower et al. 2006; Croton et al. 2006; Somerville et al. 2008), by injecting large amounts of energy into the ICM to keep the gas hot. Several other candidates to solve this problem have been suggested such as magnetic conduction (Narayan & Medvedev 2001; Fabian 2002), Type Ia supernova feedback (Sasaki 2001), and dynamical heating (Birnboim, Dekel & Neistein 2007), but the current consensus is that none of these are able to sufficiently counteract cooling (Kravtsov & Yepes 2000; Borgani et al. 2004). Meanwhile, bubbles of hot gas seemingly created by AGN jets have been observed with sufficient mechanical inflation work to counteract cooling (McNamara & Nulsen 2007) lending credence to the idea that AGN jet feedback is responsible for the heating of the ICM, which quenches massive galaxies and solves the cluster flow problem.

Modern models of groups and clusters must therefore include the impact of AGN feedback. Among hydrodynamic simulations, Illustris (Genel et al. 2014; Vogelsberger et al. 2014), Magneticum (Hirschmann et al. 2014), Horizon-AGN (Dubois et al. 2014; Volonteri et al. 2016; Kaviraj et al. 2017), EAGLE (Schaye et al.

⋆ E-mail: dylanr@roe.ac.uk (DR); rdave@ed.ac.uk (RD)

2015), MassiveBlack (Khandai et al. 2015), Blue Tides (Feng et al. 2016), Romulus (Tremmel et al. 2017), Illustris-TNG (TNG; (Springel et al. 2018), FABLE (Henden et al. 2018), and SIMBA (Davé et al. 2019) all include BH growth and the energetic output resulting from BH accretion. A plausible connection between AGN feedback and quenching of star formation was able to be established by EAGLE, TNG, FABLE, and SIMBA thanks to their success in broadly reproducing the observed massive red and dead galaxy population.

Due to the difficult nature of modelling AGN, different simulations have approached the problem in a variety of ways. EAGLE's implementation employs a single mode of AGN feedback with a fixed efficiency, injecting energy thermally at the location of the BH proportional to its accretion rate. TNG conversely employs two forms of feedback, with kinetic BH-driven winds at low accretion rates, and thermal feedback heating gas surrounding the BH at high accretion rates. FABLE employs a modified version of this, in which quasar mode feedback at high accretion rates is stored in the BH until there is enough energy to raise the temperature of a set number of particles by a given amount. Finally, SIMBA employs high-velocity jets similar to TNG, but does so in a stably bipolar fashion, and also explicitly decouples the jet material until it reaches typically several tens of kpc from the host galaxy. While the amount of energy used for AGN feedback in these models is similar, the location of the energy deposition and hence its impact on surrounding gas can be different. The nature of the torque-limited BH accretion model used in SIMBAmeans that BHs inherently grow along galaxy-BH scaling relations with no need for self-regulation (Anglés-Alcázar, Özel & Davé 2013a), allowing for a more collimated AGN feedback to enact galaxy quenching.

Observations allow us to place constraints on these varying forms of AGN feedback at low redshifts, as we explored in Robson & Davé (2020). X-rays provide an efficient and physically motivated method of detection that allows us to probe the potential well of a cluster through the observation of its X-ray luminosity, L_X. Observed properties such as L_X and the X-ray luminosity-weighted temperature T_X allow us to establish proxies for the cluster mass through the use of scaling relations. These scaling relations have been studied in great detail for low redshifts (Böhringer et al. 2007; Pratt et al. 2009; Vikhlinin et al. 2009; Arnaud et al. 2010). We are then able to use the halo mass to examine the space density of clusters, and more thoroughly test theoretical models of cluster formation.

Moving to higher redshifts, X-ray observations rapidly become more challenging owing to surface brightness dimming, making it difficult to precisely know the evolution of scaling relations with redshift (Reichert et al. 2011). Several studies have found self-similar evolution to redshift $z \sim 1$ driven primarily by the density of the Universe increasing with redshift (Vikhlinin et al. 2002; Maughan et al. 2006). Other works however have found evolution departing from that predicted by self-similarity (Ettori et al. 2004; Branchesi et al. 2007). This lack of consensus may arise from difficulties in managing selection bias in samples of high-redshift clusters drawn from different surveys. Future X-ray telescopes such as *Lynx* and *Athena* are expected to allow us to probe larger samples to higher redshifts.

Numerous cosmologically-situated hydrodynamical simulations have been used to examine X-ray scaling relations, with many of them broadly reproducing observed $L_X - M_{halo}$ relations and gas fractions (Davé, Katz & Weinberg 2002; Le Brun et al. 2014; Pike et al. 2014; Planelles et al. 2014; McCarthy et al. 2017). Mock X-ray observations from the EAGLE simulations were then analysed using observational

techniques (Schaye et al. 2015), showing good agreement versus $L_X - T_X$ observations seen for low-temperature groups, while being too high for $T_X \gtrsim 1$keV systems. Using a tuned set of parameters in which AGN provide an increased level of feedback ('AGNdT9'), Barnes et al. (2017b) simulated thirty galaxy clusters spanning $10^{14} < M_{200}/M_\odot < 10^{15.4}$, known as the Cluster-EAGLE (C-EAGLE) zooms. C-EAGLE shows better agreement with observations for $T_X - M_{500}$ and $L_X - M_{500}$, with a break seen in the luminosity scaling at group scales, but still appear too gas rich at $\sim 10^{14}\,M_\odot$. The BAHAMAS simulations (McCarthy et al. 2017) further tuned EAGLE's AGN feedback to reproduce hot gas fractions, as well as L_X and T_X versus X-ray mass, over several orders of magnitude. Still, a slight over prediction was seen in L_X values for the highest mass clusters, a trend also seen in the MACSIS suite of zoom simulations (Barnes et al. 2017a), which extend the BAHAMAS sample with 390 massive clusters. Henden, Puchwein & Sijacki (2019) studied the redshift evolution of the X-ray scaling relations of groups and clusters in the FABLE simulations and discussed three key findings. Significant deviations from self-similarity was seen for $M_{gas} - M_{halo}$, $M_{halo} - T_X$, $L_X - M_{halo}$, $L_X - T_X$, and Sunyaev−Zeldovich flux decrement. No strong evidence was predicted for the redshift evolution of these scaling relations, save for a mild steepening in the L_X relation at $z \gtrsim 0.6$ coinciding with increasing radio mode feedback in the simulations. Lastly, it was shown that normalizations of these relations evolved positively with respect to self-similarity for all investigated relations.

In Robson & Davé (2020), we found that the SIMBAsimulation is able to broadly reproduce global scaling relations at $z = 0$ in good agreement with observed stellar baryon and hot gas mass fractions as a function of halo mass, and X-ray scaling relations against both M_{500} and T_X. Profiles on the other hand show some significant discrepancies. While temperature profiles are in reasonable agreement, if a little low as suggested by Oppenheimer et al. (2021), entropy profiles are too flat towards the inner regions, with a high entropy core for intermediate mass haloes that does not match observations. In SIMBA, it was also found that the jets strongly evacuate the halo of group-sized objects which is critical for quenching the central galaxy. This echoes the results of Davies et al. (2019, 2020) using EAGLE and IllustrisTNG who found that the evacuation of gas via AGN feedback drives central galaxy quenching, despite significant differences in the way such feedback is implemented in those simulations. None the less, the overall agreement in global scaling relations suggests that SIMBA provides a broadly viable platform to explore the nature of X-ray emission from hot halo gas.

This highlights that current galaxy formation models that are successful at reproducing quenched galaxies usually have circumgalactic gas that is strongly impacted by AGN feedback. Presumably, the different models of feedback can yield differing predictions for the X-ray emission frmo hot halo gas. It is thus timely to make predictions for the expected evolution of groups and clusters within self-consistent galaxy formation models, to better understand what constraints on key physical processes such as AGN feedback are possible. By examining how the hot gas content of haloes evolves over redshift, we can hopefully constrain not only the physical processes driving AGN feedback in these dense environments, but also determine how AGN drive the evolution of intragroup and intracluster gas. For instance in simulations, it is possible to study the evolution of a set of simulated haloes over time to better understand the key physical processes leading to quenched galaxies and their surrounding hot gas.

In this paper, we examine the redshift evolution of the X-ray scaling relations of haloes in the SIMBA suite of cosmological

simulations (Davé et al. 2019). We also track how populations of haloes binned by mass evolve along these scaling relations, in order to examine how various galaxy formation processes, particularly AGN feedback, have a differential impact with halo mass. Finally, we examine these trends in test simulations where we turn-off individual feedback modules, in order to isolate the particular physics in SIMBAdriving the evolution.

This paper is organized as follows. In Section 2, we discuss the SIMBA suite of simulations and the key tools in reproducing X-ray scaling relations. In Section 3 we discuss the evolution of X-ray scaling relations from $z = 3$ to 2. In Section 4, we investigate the evolution of these scaling relations utilizing differing levels of feedback within simulations. And finally in Section 5, we discuss the evolution of profiles both within the fiducial run, and within the $50\,h^{-1}$Mpc No-Jet run of SIMBA to examine the impact of jet feedback.

2 SIMULATIONS AND ANALYSIS

2.1 The SIMBA simulation

The SIMBA simulation (Davé et al. 2019) is a cosmological hydrodynamic simulation using the GIZMOcode (Hopkins 2015). The flagship simulation evolves a random cosmological volume of $(100\,h^{-1}$ Mpc$)^3$ including 1024^3 dark matter particles and 1024^3 gas elements evolved from initial conditions to the present-day. SIMBA adopts a Lambda cold dark matter cosmology with $\Omega_\Lambda = 0.7$, $\Omega_m = 0.3$, $\Omega_b = 0.048$, $h = 0.68$, $\sigma_8 = 0.82$, and $n_s = 0.97$ in line with Planck Collaboration XIII (2016). A variable gravitational softening length is employed enclosing 64 particles, with a minimum value of $0.5\,h^{-1}$ kpc. The mass resolution is $1.82 \times 10^7\,M_\odot$ per gas element, and $9.6 \times 10^7\,M_\odot$ per dark matter particle.

Gas with hydrogen number density above 0.13 atoms cm^{-3} is assumed to lie along an equation of state with $T \propto \rho^{1/3}$ (Schaye & Dalla Vecchia 2008), and gas with temperatures less than 0.5 dex above this is considered eligible for star formation. An H_2-based model with the H_2 fraction computed from the Krumholz & Gnedin (2011) subgrid model, modified slightly as described in Davé, Thompson & Hopkins (2016), is used to model star formation from gas in a Monte Carlo fashion. Chemical enrichment is tracked from Type II supernovae (SNe), Type Ia SNe, and asymptotic giant branch (AGB) stars, tracking eleven elements (H, He, C, N, O, Ne, Mg, Si, S, Ca, Fe) during the simulation. Radiative cooling (both primordial and metal-line) and photoionization are included using GRACKLE-3.1 assuming a Haardt & Madau (2012) ionizing background, with on-the-fly self-shielding. Star formation driven galactic winds are modelled as decoupled two-phase winds with a mass-loading factor scaled to stellar mass as described by the tracking of individual particles in the FIRE zoom simulations (Anglés-Alcázar et al. 2017b). Decoupled wind particles owing to star formation feedback are temporarily disabled from interacting hydrodynamically with the surrounding medium, until they reach either a density of 0.0013 atoms cm^{-3}, their velocity relative to surrounding gas is less than the local sound speed, or they have been decoupled for 2 per cent of the Hubble time at launch.

BHs are seeded at $10^4\,M_\odot$ in galaxies that exceed stellar masses of $10^{9.5}\,M_\odot$. This choice is motivated by high-resolution simulations such as FIRE that suggest BH growth is suppressed by star formation feedback in smaller galaxies (Anglés-Alcázar et al. 2017c). Other cosmological simulations such as EAGLE and Horizon-AGN do this more self-consistently, which owes to their choice of spherical thermal star formation and AGN feedback that can disperse dense gas

near the BH; in SIMBA, we employ bipolar decoupled winds for AGN feedback (described below) that does not impact the ISM, and hence does not appropriately suppress BH growth. Because we are mostly concerned about massive galaxies and BHs here, this choice does not impact our results, but it is something that could be improved upon in the future.

There are two modes for the growing of BHs: torque-limited accretion for gas with $T < 10^5$ K (Anglés-Alcázar et al. 2017a) in which angular momentum is the primary bottleneck to accretion (Hopkins & Quataert 2011); and Bondi & Hoyle (1944) accretion from higher temperature gas. The galaxy stellar mass threshold is motivated by findings in the FIRE project simulations showing that stellar feedback strongly suppresses BH growth in low-mass galaxies (Anglés-Alcázar et al. 2017c). Assuming that dynamical friction is enough to maintain BHs near the centre of their host galaxy, BH particles are repositioned to the potential minimum of the FOF host group, provided it is found within a distance $<4 \times R_0$ where R_0 is the size of the BH kernel used to compute the accretion rate. SIMBA also includes AGN feedback, which we detail in the next section owing to its central importance in this work.

2.2 AGN feedback in SIMBA

With AGN feedback proposed as a significant mechanism in quenching star formation and contributing the the evolution of groups and clusters, simulations must take care in modelling their impact. Heckman & Best (2014) described two main modes of AGN feedback: Radiative mode at high Eddington ratios ($f_{Edd} \equiv \dot{M}_{BH}/\dot{M}_{Edd}$); and jet mode at lower f_{Edd}. SIMBA includes these two modes, plus X-ray feedback from and high-energy photon pressure. We note that the name 'jet mode' feedback is not intended to signify that we are self-consistently modeling relativistic jets from the BH accretion disc, but rather it denotes an attempt to capture the larger scale effects of radio jets of the sort seen inflating bubbles within the ICM (e.g. McNamara & Nulsen 2007). Furthermore, while we have attempted to make choices of model parameters that are reasonably concordant with current observations, some tuning of this model was required, which was primarily driven by reproducing $z \approx 0$ observations of massive quenched galaxies. Ultimately, however, our choices for AGN feedback and its parameters are designed specifically to quench massive galaxies and obtain a stellar mass function in accord with observations. This should not be regarded as a unique or fully justified solution to how galaxy quenching works, but rather as one plausible model among many that could enact quenching. Our goal in this work is to determine the effects that SIMBA's AGN feedback model has on the intragroup gas and its evolution over time, since such intragroup gas was not used as a prior constraint in any of the tuning of model parameters.

The energy output of radiative mode AGN is dominated by electromagnetic radiation emitted by the accretion discs of central super massive black holes (SMBH). The photon pressure drives multiphase winds up to speeds of $\gtrsim 1000$ km s^{-1} or more, entraining surrounding materials and as a result can include molecular (Sturm et al. 2011) and warm-ionized (Perna et al. 2017) gas.

Jet mode AGN on the other hand produce feedback in the form of collimated jets, moving at speeds of order $\sim 10^4$ km s^{-1} on large scales, and this dominates the energetic output as bulk kinetic energy. This mode is thought to be powered by the advection-dominated accretion of hot gas prevalent at low accretion, below $1-2$ per cent (Best & Heckman 2012) and the spin of SMBHs.

Significant emission from the BHs in both modes also provide a photon pressure on surrounding material. Cold gas, often found

around radiative mode AGN, is able to quickly absorb and subsequently radiate away this X-ray photon pressure. However, in systems with low cool gas fractions, the photon pressure is able to drive a spherical outward momentum.

The way in which these modes interact with their surrounding medium can have a significant impact on the growth and evolution of the galaxies and haloes in which they reside. As a result, SIMBA attempts to implement these forms of feedback in a way that mirrors observations as closely as possible. It is not only important to consider how the feedback is implemented, but when, since we are concerned here with redshift evolution.

Radiative and jet feedback in SIMBA is modelled as purely kinetic and bipolar, continuous outflows, ejected parallel to the axis of angular momentum of the inner disc. Using observations of ionized gas linewidths of X-ray detected AGN (Perna et al. 2017) the outflow velocity for radiative mode is parametrized in terms of BH mass M_{BH} (with units $M_\odot$) as

$$v_{w,EL} = 500 + 500 \left(\log \frac{M_{BH}}{M_\odot} - 6 \right) /3 \quad \text{km s}^{-1} \qquad (1)$$

This model is similar to the AGN feedback implemented in GIZMO (Anglés-Alcázar et al. 2017a), however, includes a variable outflow velocity.

As f_{Edd} drops to <0.2 the jet feedback begins to add an additional velocity component, with a strength depending on the Eddington ratio:

$$v_{w,jet} = v_{w,EL} + 7000 \log \frac{0.2}{f_{Edd}} \quad \text{km s}^{-1}, \qquad (2)$$

with the velocity increase capped to 7000 km s^{-1} at $f_{Edd} \leq 0.02$. The motivation for this arises from Heckman & Best (2014) who argue that strong radio jets only appear at Eddington ratios below $1-2$ per cent, which the choice of 0.2 for the onset of the velocity addition is made for practical purposes to avoid an abrupt threshold. We note that the velocity addition ramps up quite quickly as $f_{Edd} \rightarrow 0.02$, hence our results are not very sensitive to the onset threshold.

Additionally jet mode will only be triggered when $M_{BH} > 10^{7.5} M_\odot$, broadly following observations in which radio jets at $z \sim 1$ only occur within galaxies containing BHs with $M_{BH} \gtrsim 10^8 M_\odot$ (Barišić et al. 2017), though jets can be seen occasionally associated with lower mass BHs at $z \approx 0$ (Merloni, Heinz & di Matteo 2003; Foschini et al. 2017); if such low-mass BHs are responsible for feedback that plays an active role in quenching, then SIMBA explicitly will not accurately include such effects. In SIMBA, the onset of jet feedback is primarily governed by the f_{Edd} criterion, partly because galaxies with $M_* < 10^{9.5} M_\odot$ are not seeded with BHs. The BH seeding mass limit also has implications on when jet feedback typically begins; for instance, removing this limit would result in the onset of quenched galaxies at lower stellar masses, and a stellar mass function that is in mildly worse agreement with observations. As discussed in Davé et al. (2019), this partly arises because the BH swallowing gas particles (of mass $10^{7.26} M_\odot$) is implemented stochastically, which in small galaxies can lead to periods of low Eddington ratios owing purely to coarse numerical resolution. Implementing this limit thus avoids such low-mass galaxies from emitting jets, when their true accretion should probably be more smooth. As BHs grow in mass with time, we also see a decreasing f_{Edd} (Anglés-Alcázar, Özel & Davé 2013b), because the accretion rates have a relatively weak dependence on mass (Thomas et al. 2019). This combination of M_{BH} beginning to cross the limit of $10^{7.5}$, and a decreasing f_{Edd} we expect to see jet feedback turning on at $z \sim 1.5$ for central galaxies in group-sized haloes.

While radiative mode winds are ejected at the ISM temperature, gas in jets is raised to the virial temperature of the halo. Jets are typically observed to be made up of synchroton-emitting plasma, eventually thermalizing an around T_{vir} with surrounding hot gas (Fabian 2012). To avoid significant radiative losses in the dense gas surrounding the BH, gas wind elements undergo a short hydrodynamic and radiative cooling decoupling time of $10^{-4}t_H$, where t_H is the Hubble time at launch. The decoupling has little effect owing to the large outflow speeds, as the outflows would push through the ISM gas in any case, but it ensures that, for example, for jets the energy deposition typically happens at a few tens of kpc away from the central galaxy, roughly in the range as observed for radio jets in massive haloes. However, for radiative feedback, the recoupling can happen fairly close to the galaxy, where gas is still relatively dense and therefore numerical overcooling can be important. Hence it is possible that the impact of the radiative mode is underestimated in SIMBA's model. Finally, we note that the metal content of the gas particle is unchanged upon launch in AGN feedback, and all metals locked into dust are added back into the gas phase.

X-ray feedback operates in two forms, depending on the gas it is heating. Non-ISM gas is heated directly according to the heating flux. ISM gas however is low resolution, so any added heat would quickly be cooled away. Thus, one-half of the energy is applied as a radial outward kick with the other being added as heat. X-ray feedback is only activated at low eddington ratios ($f_{Edd} < 0.02$) alongside full velocity jets. This aims to crudely mimic the idea that high Eddington ratio systems have a surrounding gas torus that would absorb the X-rays. In an attempt to model the ability of the gas rich ISM to further absorb and radiate X-ray energy, galaxies must also have a cold gas fraction of $f_{gas} < 0.2$, and the strength of the X-ray feedback scales linearly with $0.2 - f_{gas}$. Without this, small galaxies that temporarily have low Eddington ratios owing to stochasticity in the accretion can emit X-ray feedback, which can yield a temporary suppression of star formation in small gas-rich systems that is likely purely numerical. X-ray feedback has a minimal effect on the galaxy mass function, however, it contributes to fully quenching galaxies (Davé et al. 2019).

Alongside the fiducial $100 h^{-1}$Mpc box, we have also run a number of 'feedback variant' runs excluding various modules of the implemented feedback. Due to the computational requirements of running these simulations, these runs use a $50 h^{-1}$Mpc box with 512^3 dark matter particles and 512^3 gas elements. This gives these runs the same resolution as the fiducial run, with one-eighth the volume. The initial conditions for all $50 h^{-1}$Mpc runs are identical. While this reduces the number of high-mass haloes, we are still able to examine the impact of the various forms of feedback amongst group-sized haloes. The feedback variant run turn-off one aspect of feedback at a time, in turn, as follows:

(i) a 'No-X' model (SIMBA-NoX) with only X-ray feedback turned off and jets are left on;
(ii) a 'No-Jet' model (SIMBA-NoJet) with jet and associated X-ray feedback turned off;
(iii) a 'No-AGN' model in which all AGN feedback is turned off; and finally; and
(iv) a 'No-Feedback' model in which all feedback including star formation winds is turned off.

We note that the parameter choices are tuned to reproduce galaxy mass functions across cosmic time, which particularly require effective quenching in massive galaxies. Certainly, other models with other parameters can be equivalently effective at this, such as EAGLE (Schaye et al. 2015) and IllustrisTNG (Pillepich et al. 2018). Here, our motivation is to examine the X-ray properties of

hot gas within massive haloes, which was not used as a constraint on the feedback models. Thus although our results are tied to a specific model as implemented in SIMBA, they represent a viable model within which to examine the evolution of X-ray group properties.

2.3 Identifying haloes and computing X-ray emission

Halos are identified via a 3D friends-of-friends (FoF) finder implemented within GIZMO, using a linking length that is 0.2 times the mean interparticle spacing. Galaxies are identified in post-processing from within these haloes, using a 6D FoF finder applied to star-forming gas and stars. The galaxies and haloes are identified and catalogued using the CAESAR code (Thompson 2015). These catalogues, along with particle snapshots, for all the runs described above are publicly available at simba.roe.ac.uk.

The python package PYGAD (Röttgers et al. 2020) is a multipurpose analysis toolkit for particle-based hydrodynamics simulations, and gives us tools for the general analysis of simulations. Various criteria such as specific particles, defined regions, or particles that fit within a specified parameter range (e.g. temperature or metallicity) can be used to create sub-snapshots with particles contained within individual CAESAR haloes.

A module for analysing X-ray luminosity is included in PYGAD, using XSPEC (Arnaud et al. 2010) to compute X-ray spectra. XSPEC is fully described in Eisenreich et al. (2017). PYGAD calculates the X-ray luminosity of selected gas particles using emission tables in XSPEC along with particle temperatures and metallicities taken from the simulation. XSPEC uses the APEC emissivity tables, while cooling rates in the simulation use CLOUDY tables. Differing cooling rates will result in the post-processed cooling rates to be slightly incompatible with the simulated ones, the result of which is likely to be an overestimate of the post-processed cooling rates and hence the luminosity. In practice, this error is likely to be small when averaged over the many gas particles in a cluster, so we follow common practice in this field and ignore it. In our analysis of SIMBA's X-ray properties, we use the 0.5–2-keV X-ray table to be consistent with the work done in Robson & Davé (2020). PYGAD is publicly available at https://bitbucket.org/broett/pygad.

We choose to use the rest-frame 0.5−2-keV band at all redshifts, which means that our $z > 0$ predictions are not directly comparable to observations owing to the redshifting of the bandpass. The primary reason for this choice is that we wish to examine the intrinsic evolution of group X-ray properties, without the complication of bandpass shifts. Given the scarcity of higher redshift data on group X-ray properties, it seems in any case premature to engage in detailed observational comparisons. Instead, by focusing on the rest-frame evolution, we can see how the emergence of hot gas within massive haloes is manifest in its X-ray properties. Furthermore, we can more robustly explore comparisons between the SIMBA feedback variants, in order to identify which feedback aspects are the most crucial drivers of evolution. In the future, we plan to make more details predictions in the observational plane specifically targeting future X-ray surveys including observational effects, which is a significant effort that is beyond the scope of the current work.

In the end, we identify 1379, 1051, 509, and 126 haloes with $M_{500} > 10^{12.3}\,\mathrm{M_\odot}$ at $z = 0, 1, 2, 3$, respectively, in our flagship run. This constitutes the main sample that we will analyse for this work.

3 EVOLUTION OF SCALING RELATIONS

We begin by examining the evolution of X-ray scaling relations in our selected galaxy groups. Intragroup gas can be characterized by
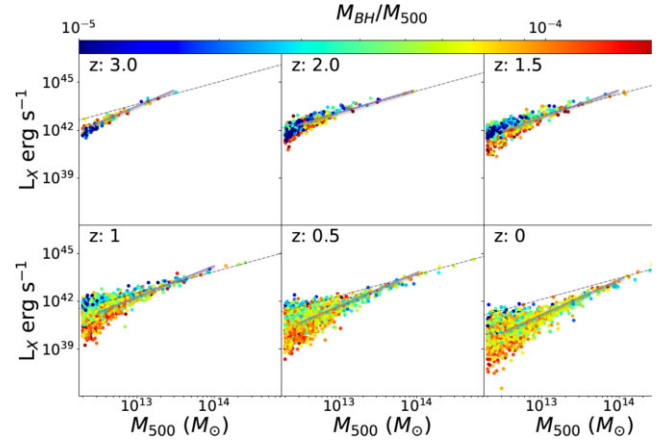
Figure 1. $L_X - M_{500}$ scaling relation for rest-frame 0.5−2 keV from $z = 3 \rightarrow 0$. Colourbar is scaled as M_{BH}/M_{500}. The nominal self-similar scaling ($L_X \propto M_{500}^{1.5}$) normalized to the most massive haloes is shown by the dashed line. The semi-transparent purple line shows the best-fit power law between $10^{12.5} \leq M_{500} \leq 10^{14}\,\mathrm{M_\odot}$. The slope of the scaling relation shows modest evolution, from roughly self-similar (1.5) at $z = 1.5-2$, increasing to ≈ 1.8 at $z = 1$ and ≈ 2 at the lowest redshifts. As we move from $z = 3$ to 0 the most luminous haloes appear to increase in mass, while the smallest haloes drop in luminosity. A significant increase in scatter is also seen in haloes with $M_{500} < 10^{13}\,\mathrm{M_\odot}$, being ≈ 0.4 dex at $z \geq 1.5$ but ≈ 1 dex at $z \leq 0.5$. At $z \lesssim 1.5$ lower L_X haloes at a given mass have noticeably higher typical f_{BH}.okok

its X-ray luminosity L_X, X-ray luminosity-weighted temperature is T_X, the hot gas fraction is f_{gas}, and the X-ray luminosity-weighted metallicity is Z_X. To understand the physical drivers behind these relations, we first examine the evolution with respect to M_{500}, both by looking at the scaling relations at various redshifts, and by tracking individual haloes back in time. In the end, we make predictions for the evolution in the most common observable barometer of hot bound gas, the $L_X - T_X$ relation, and use the evolution in the physical quantities versus M_{500} to provide a context for the predicted evolution in $L_X - T_X$.

3.1 $L_X - M_{500}$ evolution

Fig. 1 shows the $L_X - M_{500}$ scaling relation for all haloes with $M_{\mathrm{halo}} > 10^{12.3}\,\mathrm{M_\odot}$ in SIMBA at $z = 3, 2.5, 2, 1.5, 1, 0.5, 0$. Points coloured by the BH mass fraction $f_{BH} \equiv M_{BH}/M_{500}$, where M_{BH} is the BH mass of the central galaxy. The dashed line shows the scaling predicted from the self-similar model ($L_X \propto M_{500}^{4/3}$), normalized to the most massive halo at that epoch. The purple line shows the best-fitting log-linear relation for haloes with $10^{12.5} \leq M_{500} \leq 10^{14}\,\mathrm{M_\odot}$.

A clear $L_X - M_{500}$ is already in place at high redshifts, even though the haloes are still relatively small. As time progresses, the best-fit slope steepens away from self-similarity at $z = 2$ to $\sim L_X \propto M_{500}^2$ at the $z \sim 0.5-0$. This demonstrates that the onset of widespread AGN feedback at $z \sim 1-1.5$ causes a significant departure from self-similarity, as expected. The best-fit also deviates from self-similarity somewhat at $z = 3$, which is likely owes to high-z low-mass haloes having such short cooling times that they cannot sustain as much hot gas; we will verify this when we explore gas fractions.

The scatter around the best-fitting relation also appears to increase with time, particularly at lower masses. At high-z, a rough estimate of the scatter is typically $\sigma \approx 0.3-0.5$ dex at all masses. At any given redshift, the most luminous X-ray haloes at a given M_{500} follow self-similarity, but there is an increasing number of haloes that deviate strongly from it. By $z \lesssim 0.5$, the scatter appears to remain similar
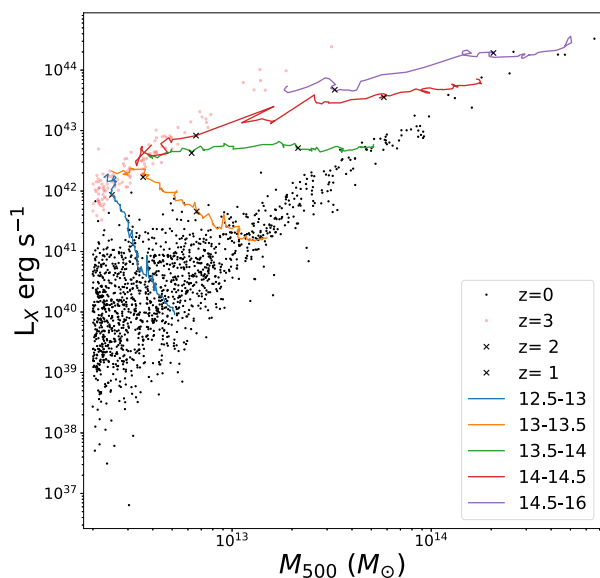
Figure 2. A plot showing the median evolution of a halo from $z = 3 \rightarrow 0$, binned by final M_{500}, with blue, yellow, green, red, and finally purple representing the least to most massive mass bins. Cross (x) marks along the tracks indicate the time of $z = 2$ and 1 on each track. Red and black dots represent the haloes at $z = 3$ and 0, respectively. Halos with final masses $\gtrsim 10^{13.5}\,M_\odot$ show little change in luminosity over an order of magnitude increase in M_{500}. In contrast, haloes with final masses $< 10^{13}\,M_\odot$ show an order of magnitude or more decrease in luminosity for only a modest increase in mass.

to that at high redshifts for $M_{500} \gtrsim 10^{13.5}\,M_\odot$, but for lower mass haloes it seems closer to $\sigma \sim 1$ dex. This suggests that stochastic feedback within group-sized haloes translates into a higher spread in the L_X-M_{500} relation.

The scatter is further correlated with f_{BH} of lower mass haloes. From $z = 2 \rightarrow 0$, we see that the lowest L_X haloes at any given mass tend to have the highest f_{BH}. Indeed, the galaxies with very low f_{BH} tend to lie near self-similarity all the way down to $z = 0$, even at the lowest halo masses probed. This implicates processes related to growing large BHs as the primary driver for departures from self-similarity.

These results can be understood by appealing to the impact of AGN jet feedback in SIMBA. As noted earlier, jet feedback turns on at low f_{Edd}. As shown in Anglés-Alcázar et al. (2013a), at these mass scales, the Eddington ratio becomes comparable to the jet threshold at $z \sim 1.5$, albeit with a fair amount of scatter. Thus, we expect that BHs that have managed to grow large by these epochs will be putting out a significant fraction of their AGN feedback in high-energy jets into intragroup gas. This circumstantially correlates well with driving a decreasing L_X in systems with large f_{BH} at $z \lesssim 1.5$. We will show more evidence for this connection with AGN jet feedback when examining the other scaling relations.

Fig. 2 provide another view on how the $z = 3$ population evolves to $z = 0$. Here, we examine the median evolutionary tracks of haloes binned by final ($z = 0$) halo mass. The small points are in two groupings: The high-L_X grouping (red points) shows individual haloes at $z = 3$ while the low grouping (black points) shows haloes at $z = 0$. The coloured lines show median tracks of haloes in various $z = 0$ M_{500} bins: $M_{500} > 10^{14.5}\,M_\odot$ (purple), $10^{14} < M_{500} < 10^{14.5}\,M_\odot$ (red), $10^{13.5} < M_{500} < 10^{14}\,M_\odot$ (green), $10^{13} < M_{500} < 10^{13.5}\,M_\odot$
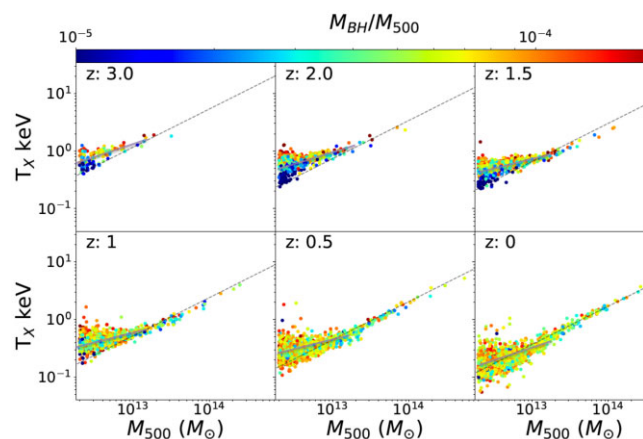

Figure 3. T_X-M_{500} scaling relation from $z = 3 \rightarrow 0$ at intervals of 0.5. The colourbar is scaled as log M_{BH}/M_{500}. The expected self-similar scaling normalized to the most massive haloes is shown by the dashed line. The purple line shows the best-fitting power law for $M_{500} < 10^{13.3}\,M_\odot$, which is always shallower than self-similar; above this mass, the best fits are all consistent with self-similarity. The relation shows an increasing scatter at low masses towards higher T_X, which at $z \gtrsim 1.5$ is well correlated with the BH mass, but at lower redshifts it is not. This suggests that BH feedback in low-mass haloes dominates halo gas heating at early epochs.

(gold), $10^{12.5} < M_{500} < 10^{13}\,M_\odot$ (blue). These are constructed by following individual haloes back in time via their most massive dark matter progenitor, so long as the progenitor has $M_{500} > 10^{12.5}\,M_\odot$.

This shows that haloes with $z = 0$ $M_{500} > 10^{13.5}\,M_\odot$ show little change in L_X despite an order of magnitude or more increase in M_{500} from $z = 3$ to 0. In contrast, haloes with a $z = 0$ $M_{500} < 10^{13.5}$ show an order of magnitude or more decrease in L_X, with a smaller increase in mass. Interestingly, the slope of the relation evolves relatively modestly, despite the dramatically mass-dependent behaviour. As a result, the evolution of L_X-M_{500} is not well described by an overall shift in either L_X or M_{500}, but rather a combination of effects that results in the L_X scaling relation spreading out in M_{500} over time.

We checked that including only $z = 0$ haloes with progenitors all the way back to $z = 3$ revealed similar trend in the median tracks. However, if one only follows the main descendants of haloes from $z = 3 \rightarrow 0$, this reveals that individual scaling tracks almost exclusively retain a constant luminosity as mass increases from $z = 3$ to 0. This indicates that the L_X-M_{500} relation evolves via a combination of massive haloes gaining hot gas compensated by the lowering density of the cosmos, along with low-mass haloes entering into our sample above our mass cut but containing less hot gas. We will later show that this owes primarily to jet feedback removing hot gas from these lower mass haloes, as found in Robson & Davé (2020).

3.2 $T_X - M_{500}$ evolution

Fig. 3 shows the $T_X - M_{500}$ scaling relation at $z = 3, 2.5, 2, 1.5, 1, 0.5, 0$ with points colour coded by $f_{BH} = M_{BH}/M_{500}$, similar to Fig. 1. The self-similar relation is again shown as the dashed line in each panel. We show a best-fitting power-law relation for $10^{12.3} < M_{500} < 10^{13.3}\,M_\odot$ as the purple line in each panel.

We find that the T_X-M_{500} relation shows a double power law behaviour. For larger haloes with $M_{500} > 10^{13.3}\,M_\odot$, at all redshifts the relationship is consistent with the self-similar scaling of $T_X \propto M_{500}^{2/3}$ (except $z = 3$ where there are only two haloes above this mass), and the scatter is quite low, typically $\lesssim 0.05$ dex. For this
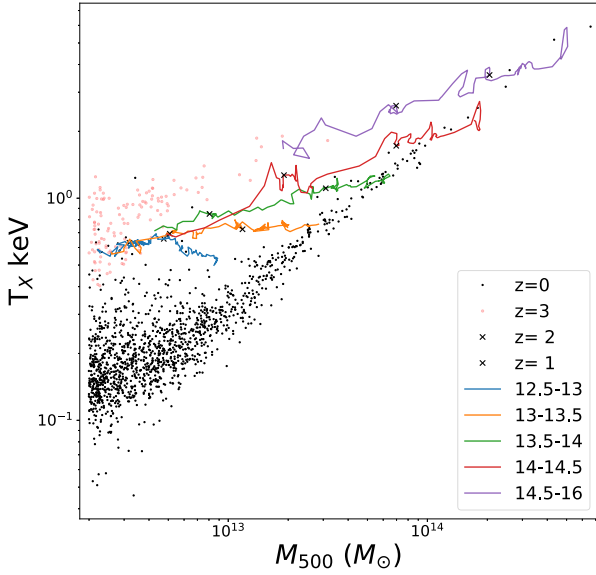
Figure 4. Median evolution of a halo from $z = 3 \rightarrow 0$, binned by final M_{500} with blue, yellow, green, red, and finally purple representing least to most massive mass bins. X marks indicate the positions of $z = 2$ and 1 on each track. Light grey dots represent the scaling relation at $z = 3$ while black dots represent the scaling relation at $z = 0$. All but the least massive bin show a clear increase in T_X. All but the most massive bin seem to originate from the same area at $z = 3$ suggesting there is no clear evolution by population based on T_X alone.

regime, we do not show the fit, and only show the power-law fit for $M_{500} \leq 10^{13.3}\,\mathrm{M_\odot}$ as the purple line. Here, the best-fitting relation is substantially shallower, and the scatter increases. The slope is ∼0.5 from $z = 2 \rightarrow 0.5$, and then steepens slightly to 0.6 at $z = 0$. The scatter about the best fit ranges from $0.1-0.3$ dex, increasing towards lower masses and redshifts, with the lower envelope of T_X values generally following self-similarity. This can be understood as heating from SIMBA's jet feedback being primarily responsible for deviations from self-similarity, and that such heating tends to be more impactful in lower mass systems with smaller potential wells, but this can also be stochastic.

The connection with BHs is further elucidated by looking at the trends with f_{BH} shown by the colour-coding. However, the situation is not as clear as in the $L_X - M_{500}$ case. At high redshifts, there is a clear trend that high-f_{BH} haloes have high T_X, and that the groups close to self-similarity are the ones with the smallest central galaxy BHs. This makes sense because the integrated AGN feedback energy is higher for high-mass BHs. Yet, the trend disappears at $z \lesssim 1$. This suggests that something is breaking the relation between T_X and M_{BH} amongst smaller haloes. One possible explanation is that jet feedback expels the hottest gas out of low-mass haloes altogether at $z \lesssim 1$, leaving only (relatively) cooler gas, and muddying the trend. Another possibility is that at lower redshifts, shock heating in the IGM from both structure formation and cumulative jet energy becomes more prevalent (e.g. Christiansen et al. 2019), and hence the impact of the AGN feedback heating associated with the central BH is diluted. We will explore these ideas more in future work, but the net result is that there is not a simple relationship with f_{BH} for the T_X-M_{500} scaling; in SIMBA, greater AGN feedback does not monotonically increase T_X at $z \lesssim 1$.

Fig. 4 shows median tracks within different halo mass bins, tracked backwards in time from the $z = 0$ population, analogous to Fig. 2.
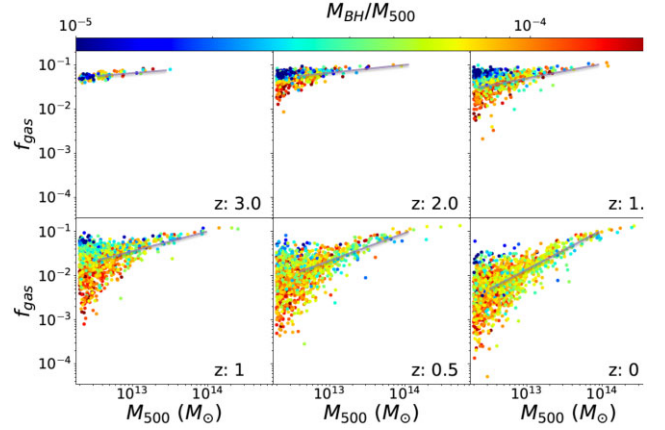
Figure 5. $f_{gas}-M_{500}$ scaling relation from $z = 3 \rightarrow 0$ at intervals of 0.5. The colourbar is scaled as log M_{BH}/M_{500} going from red to blue. The purple line shows a best-fitting power law for $10^{12.5} \leq M_{halo} \leq 10^{14}\,\mathrm{M_\odot}$. A small evolution in scatter of the least massive haloes is seen as M_{500} increases up to $z = 1.5$. After $z = 1.5$, we see a large increase in scatter at the low mass end with a significant decrease in hot gas mass fraction at these masses. This coincides with the switch on of jet feedback. Halos with $M_{500} < 10^{13.5}\,\mathrm{M_\odot}$ show higher M_{BH} corresponding to lower f_{gas}. The trends qualitatively mimic that in $L_X - M_{500}$ (Fig. 1), showing that the evolutionary trends in L_X are driven primarily by gas fractions.

Again, we show five $z = 0$ halo mass bins in M_{500} as denoted in the legend. The tracks start at $z = 3$ on the left-hand side and evolve rightwards (growing in M_{500}) with time, and we show cross marks along the tracks at $z = 1, 2$.

We see that the evolution here has some similarities but also some differences relative to the tracks in L_X-M_{500} space. The highest mass haloes show a clear increase in temperature from $z = 3 \rightarrow 0$, while the least massive haloes at $z = 3$ show less change in the X-ray weighted gas temperature. Interestingly, all haloes start along the same mildly upwards trend, but while the massive haloes continue that trend to $z = 0$, at $z \lesssim 1$ the low-mass haloes stop evolving in T_X, with the lowest mass bin actually dropping in median T_X since $z \sim 1$. The net effect is a slight steepening of the T_X-M_{500} slope. Overall, while the slope of the relation remains relatively constant over time, the evolution of individual is not well described by a simply evolution in either T_X or M_{500}, but a combination of effects that results in groups spreading out in $T_X - M_{500}$ over time.

This differential evolution with halo mass is likely driven by the interplay between jet feedback and structure formation. At the lower masses, the jets are fast enough to drive substantial material out of haloes, heating the surrounding gas but depositing less energy into the halo itself. At the higher masses, the jets cannot escape the halo as easily, and the kinetic energy is thermalized within the halo.

3.3 $f_{gas}-M_{500}$ evolution

In examining L_X and T_X versus M_{500}, we have implicated the halo hot gas fraction f_{gas} as an important quantity that is directly impacted by jet feedback. Robson & Davé (2020) showed that without jets on, gas fractions show much larger values in small haloes, with not nearly as strong a trend with halo mass. Thus, it is worth examining how the gas fraction evolves with time, to provide insights into the evolution of other more directly observable quantities.

Fig. 5 shows the $f_{gas}-M_{500}$ scaling relation at $z = 3$, 2.5, 2, 1.5, 1, 0.5, 0 with points colour-coded by $f_{BH} = M_{BH}/M_{500}$. We note that the top of each panel corresponds to f_{gas} reaching the cosmic halo

Figure 7. $Z_X - M_{500}$ scaling relation from $z = 3$ to 0 at intervals of 0.5. The colourbar is scaled as f_{star} from 0 to 0.1 going from red to blue. A clear increase in metallicity is seen at the low mass end.
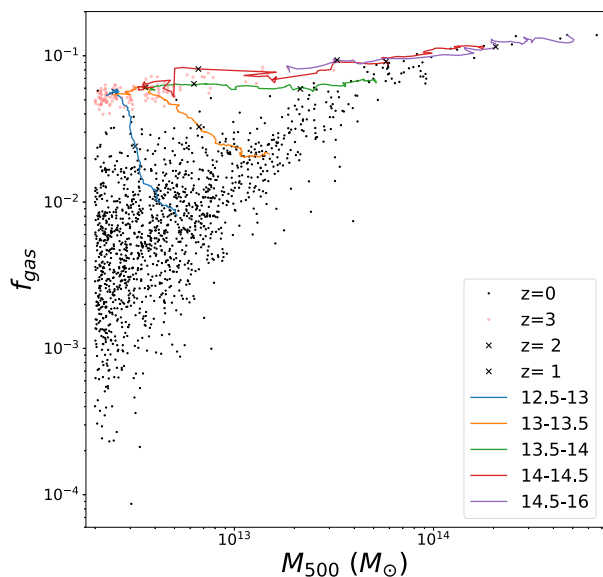
Figure 6. A plot showing the median evolution of a halo from $z = 3 \rightarrow$ 0, binned by final M_{500} with blue, yellow, green, red, and finally purple representing least to most massive mass bins. X marks indicate the positions of $z = 2$ and 1 on each track. Light grey dots represent the scaling relation at $z = 3$ while black dots represent the scaling relation at $z = 0$. Halos with M_{500} $< 10^{13.5}\,\mathrm{M_\odot}$ show a clear drop in f_{gas}, showing that SIMBA's jet feedback is working to remove hot gas from the least massive haloes.

baryon fraction Ω_b/Ω_m. We define hot gas as gas with $T > 10^{5.5}$ K, though our conclusions are not sensitive to this definition to within ± 0.5 dex.

From $z = 3 \rightarrow 1.5$, we see that f_{gas} has a fairly weak trend with halo mass. As time goes and particularly at $z \lesssim 1.5$, the scatter increases substantially towards the low-mass end, with an increasing number of haloes with lower f_{gas} values. This scatter introduced at lower masses results in a steepening of the $f_{gas} - M_{500}$ scaling relation. The best-fitting slope for $10^{12.5} \leq M_{halo} \leq 10^{14}\,\mathrm{M_\odot}$ haloes (purple line) increases steadily from ≈ 0.1 at $z \geq 2$ to 0.82 at $z = 0$. Although we do not show an observational comparison here, Davé et al. (2019) and Robson & Davé (2020) showed that this trend is in reasonable agreement with observations at $z = 0$.

The colour scaling shows an inverse relation between f_{BH} and f_{gas} at $M_{500} < 10^{13.5}\,\mathrm{M_\odot}$, with lower BH fractions corresponding to higher hot gas fractions. This trend is already beginning at $z = 2$, showing the effects of early jet feedback that results in early quenched galaxies (Stevans et al. 2021), with the effects ramping up most strongly from $z = 2 \rightarrow 1.5$. The lower hot gas content in haloes with more AGN feedback might seem counterintuitive, since one expects AGN feedback to heat gas. But the wind speed of the jets is such that it can easily unbind gas at these lowest masses, whereas for the high-mass haloes it will be more easily trapped within the halo. Thus the impact of AGN jets is not so much to heat the halo gas, as expel it. This is why we see a correspondingly strong trend with f_{BH} in L_X which is sensitive to gas density, but a weak trend with T_X. We will examine gas densities later when we look at the X-ray profiles.

Fig. 6 tracks the gas fraction over time for these haloes. We see that it is only the less massive haloes showing a decrease in f_{gas} with haloes of $M_{500} > 10^{13.5}\,\mathrm{M_\odot}$ demonstrating steady or mildly increasing f_{gas}. This trend is qualitatively similar to what was seen in tracking L_X (Fig. 2), highlighting the direct impact of f_{gas} on L_X.
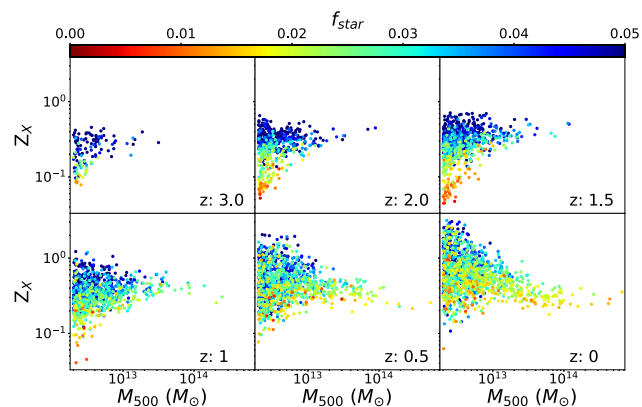
3.4 $Z_X - M_{500}$ evolution

While emission via bremsstrahlung dominates for systems with $T_X \gtrsim 1$ keV metal-line emission becomes increasingly important towards lower T_X systems. This includes the majority of systems in our sample, and as such an examination of the hot gas metallicity of these systems also provides insight. Moreover, metals provide a unique tracer of supernova-generated products and their distribution into intragroup gas.

Fig. 7 shows the $Z_X - M_{500}$ scaling relation at $z = 3$, 2.5, 2.0, 1.5, 1.0, 0.5, 0 with points scaled by the stellar mass fraction f_{star}. f_{star} here is defined as the ratio of stellar mass within R_{500} against M_{500}. Through f_{star} we can infer a level of stellar feedback within a cluster, a key driver behind metallicity. Scaling by M_{BH}/M_{500}, as in previous plots, showed no relation motivating us to investigate the effects of different forms of feedback on evolution.

Between $z = 3$ and 1.5 little evolution is seen in the shape of the relation, with an increase in haloes above the mass cut we see little change in metallicity at any given mass with the exception of more massive haloes become present. However after $z < 1.5$ we begin to see a change in metallicities seen among low-mass haloes. Much like previous scaling relations, we see an increase is seen in the scatter at lower masses. In particular, the lowest mass groups can show high intragroup metallicities, exceeding solar in some cases at $M_{500} < 10^{13}\,\mathrm{M_\odot}$.

Noting the colour coding, the high intragroup metallicities correlate fairly well with high f_{star} in the central galaxy. This trend is very pronounced at high z, but remains noticeable all the way to $z = 0$. At $z > 1$, the lowest metallicity systems have very low stellar fractions, which suggests that these systems have been quenched early on (Cui et al. 2021). This is perhaps not surprising, since the stars are responsible for producing much of the metals in the system, particularly early on. Moving to lower redshifts, if re-accretion of enriched intergalactic gas (i.e. 'outside-in enrichment'; Oppenheimer et al. 2012) imparts a metal floor in these high-density environments in SIMBA as we expect from previous simulations, this would dilute the strong trend arising purely from self-enrichment. None the less SIMBA predicts that poor groups with higher stellar masses (which also tend to have more star-forming galaxies; Cui et al. 2021) will generally have higher metallicities.
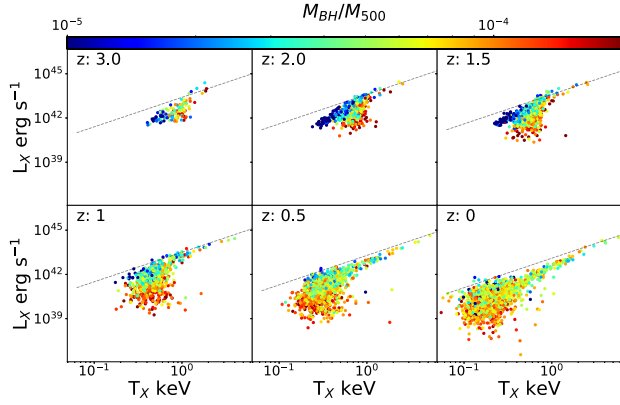
Figure 8. $T_X - L_X$ scaling relation from $z = 3$ to 0 at intervals of 0.5. The colourbar is scaled as M_{BH}/M_{500}. The expected self-similar scaling normalize to the most massive haloes is shown by the dashed line. A tight scaling is retained amongst the hottest most luminous haloes, however, a large scatter is introduced at low temperatures and luminosities. The introduction of jet feedback after $z = 1.5$ coincides with the introduction of a number of low-temperature, low-luminosity haloes exhibiting a large scatter.

3.5 $L_X - T_X$ evolution

The $L_X - T_X$ relation has long been a key observational diagnostic of hot gas in massive haloes. The evolution of this relation will obviously be a combination of the evolution in each quantity versus M_{500} from the previous sections. Here, we examine this evolution directly, including examining how groups at different masses evolve within $L_X - T_X$ space. We remind the reader that the X-ray properties are computed in the rest-frame $0.5 - 2$-keV band, so are not directly comparable to observations in this band at $z > 0$, but they provide insight into the nature of predicted hot gas evolution without the additional complication of bandpass redshifting.

Fig. 8 shows the $L_X - T_X$ scaling relation at $z = 3$, 2.5, 2, 1.5, 1, 0.5, 0 with points colour-coded by M_{BH}/M_{500}. We impose a mass cut of $M_{500} > 10^{12.3} \, \mathrm{M_\odot}$ at each redshift. The dashed line shows the self-similar relation normalized to the highest T_X group.

From $z = 3 \rightarrow 1.5$, the $L_X - T_X$ relation looks broadly very similar, albeit with an increasing number of objects. The largest haloes with the highest T_X are already on the self-similar relation, and by $z \sim 1$ there is a fairly tight locus which sets an upper edge following self-similarity. Over time, there is a growing scatter of points to lower L_X. This becomes particularly prominent at $z \sim 1 - 1.5$ in the lower mass haloes. We have similarly seen in $L_X - M_{500}$ and $T_X - M_{500}$ scaling relations that there is a change in evolution for lower mass groups around this epoch.

There is a marked trend that the groups with the lowest L_X values have the highest f_{BH} values. This directly implicates the impact of AGN feedback in growing a population of low-mass groups that deviates from self-similarity. As we discussed earlier, the effect of the jets is to evacuate the low-mass haloes. This lowers the amount of X-ray emitting gas and thus L_X, but we showed that it does not have a strong impact on T_X values in low-mass systems because there is the competing effect that the hottest gas is evacuated from these systems altogether; we will more explicitly demonstrate this in Section 4, in which we show that jet feedback has a dramatic impact on hot gas fractions (Fig. 10) but a modest impact on T_X (Fig. 12). SIMBA's prediction of a strong anticorrelation between L_X and f_{BH} at $T_X \lesssim 1$ keV can be tested with next-generation X-ray facilities.
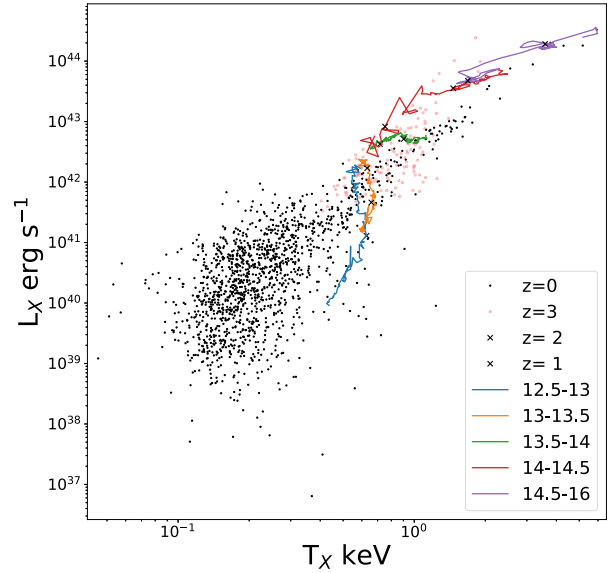

Figure 9. A plot showing the median evolution of a halo from $z = 3$ to 0, binned by final M_{500} with blue, yellow, green, red, and finally purple representing least to most massive mass bins. X marks indicate the positions of $z = 2$ and 1 on each track. Light grey dots represent the scaling relation at $z = 3$ while black dots represent the scaling relation at $z = 0$. Halos with $M_{500} > 10^{13} \, \mathrm{M_\odot}$ show little evolution in the $L_X - T_X$ space, however, the least massive haloes below this threshold demonstrate a drop of nearly two orders of magnitude in L_X while maintaining a consistent T_X.
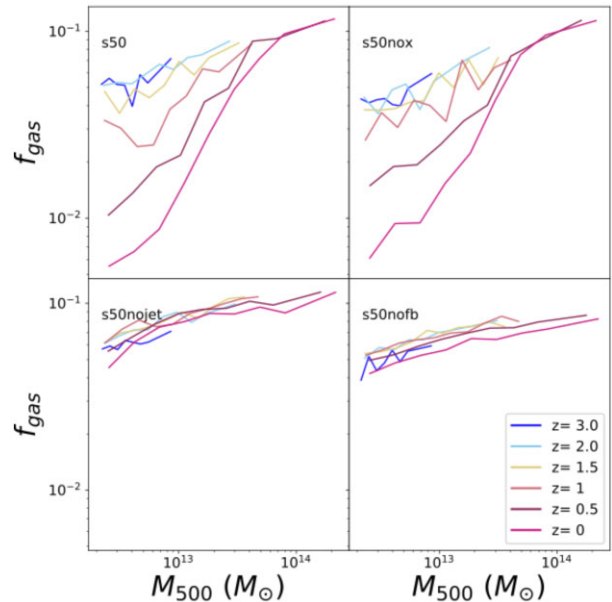

Figure 10. Evolution from $z = 3$ to 0 of the running median of the $f_{gas} - M_{500}$ scaling relation for SIMBA, SIMBA without X-ray feedback, SIMBA without jet feedback, and SIMBA with no feedback. All models lacking jet feedback (No-Jet, No-AGN, No-Feedback) show no evolution in f_{gas} while both models including jet feedback (SIMBA, No-X) exhibit a very large drop in f_{gas} in the haloes with $M_{500} < 10^{13.5} \, \mathrm{M_\odot}$.
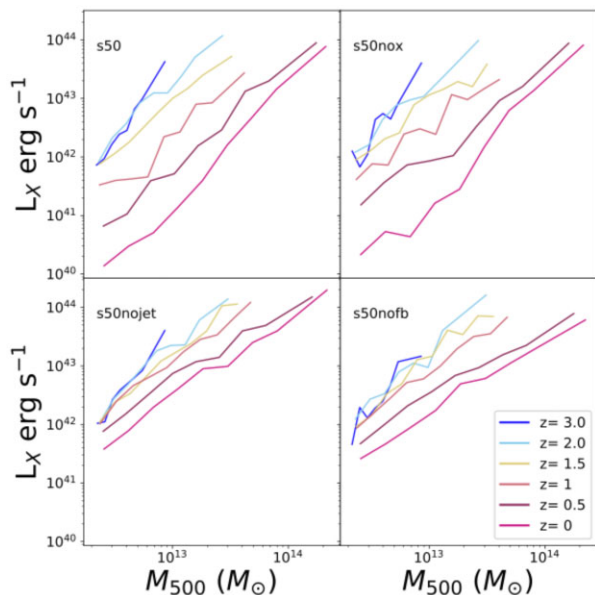
Figure 11. Evolution from $z = 3$ to 0 of the running median of the $L_X - M_{500}$ scaling relation for Simba, Simba without X-ray feedback, Simba without jet feedback, and Simba with no feedback. Little change is seen between the No-Feedback, No-AGN, and No-Jet runs, with the No-X and Simba runs exhibiting similar larger evolutions. The key difference here being the inclusion of jet feedback driving the evolution of the scaling relation.

In Fig. 9, we show the evolution of the $L_X - T_X$ relation in five $z = 0$ log M_{500} mass bins as indicated in the legend, as in previous figures. In $L_X - T_X$ space, the red points depicting $z = 3$ values are not wholly distinct from the $z = 0$ black points, since there is not a monotonic increase in T_X as there is in M_{500}.

The scaling tracks offer a very interesting perspective on $L_X - T_X$ evolution. The overall relation at $z = 3$ and 0 are not that different in terms of the slope and amplitude, although at $z = 0$ there are many more low-T_X systems with a large scatter in L_X. The apparent lack of evolution in the $L_X - T_X$ relation has been noted in some observations of clusters (Borgani et al. 2001; Holden et al. 2002), though not for lower mass groups since current X-ray data lacks the sensitivity at $z \gg 0$. Several other studies have shown this weak evolution at $z > 0.3$, however, show varying levels of evolution from $z = 0.3 \rightarrow z = 0$ motivated by the consideration of the effect of cool core clusters (Vikhlinin et al. 2002; Ettori et al. 2004).

The modest evolution in $L_X - T_X$ is seen across all masses, though again there is a different trend for $M_{500} \gtrsim 10^{14} M_\odot$ systems that tend to evolve rightwards with a modest increase in L_X, while $M_{500} \lesssim 10^{13.5} M_\odot$ evolve downwards in L_X with little change in T_X. The net effect is to leave the overall relation relatively unchanged, but to spread out the groups along the relation. Hence even though $L_X - M_{500}$ and $T_X - M_{500}$ individually show significant change over time, the $L_X - T_X$ relation combines these two coincidentally into a nearly non-evolving relation, albeit with a large increase in scatter at $T_X \lesssim 0.7$ keV.

4 EFFECTS OF FEEDBACK ON SCALING RELATIONS

We have implicated jet feedback in driving the evolution of the intragroup medium scaling relations particularly at the low-M_{500} end. We can test this more directly by examining a suite of smaller $50\,h^{-1}$Mpc runs having the same resolution, with individual AGN

and star formation modules turned on and off. This offers us the chance to directly connect the scaling relations to the physics of the implemented feedback processes.

As previously described, the variant models used for comparison are the full Simba, No-X, No-Jet, No-AGN, and No-Feedback models. No-X turns off only X-ray feedback, No-Jet additionally turns off jet feedback, No-AGN additionally turns off radiative AGN feedback, and No-Feedback additionally turns off star formation winds. Overall, the No-AGN results were very similar to the No-Jet results, showing that the radiative AGN feedback has minimal effect on X-ray scaling relations (as likewise found for galaxy properties; Davé et al. 2019), and as such it has been left out of the following plots for brevity. By investigating the evolution of scaling relations with each feedback variant run we are able to demonstrate each specific model's impact on each of the previously studied scaling relations.

4.1 Hot gas fraction

Since the hot gas fraction is implicated in driving much of the evolution of the scaling relations, we begin by examining how feedback impacts this quantity.

Fig. 10 shows the median f_{gas} as a function of M_{500} at redshifts $z = 3 \rightarrow 0$ (blue to red) in various colours as indicated in the legend. The upper left-hand panel shows a $50\,h^{-1}$Mpc run with full Simba physics, and the other panels show the No-X run (upper right-hand panel), No-Jet (lower left-hand panel), and No-Feedback (lower right-hand panel).

There is a dramatic difference in the evolution of f_{gas} once the jet feedback is turned on, seen by comparing No-Jet in the lower left, and No-X in the upper right. Turning on star formation feedback and X-ray AGN feedback have in contrast a fairly minor effect. We clearly see the impact of jet feedback at $M_{500} < 10^{13.5} M_\odot$ at $z \lesssim 1.5$ while having a limited effect at $M_{500} \gtrsim 10^{13.5} M_\odot$. Once jets are turned off (No-Jet and No-Feedback runs), there is essentially no evolution in f_{gas}. This clearly demonstrates that it is jets that are responsible for evacuating the hot gas from haloes.

The most notable evolution occurs at $z \sim 1 - 1.5$, which is consistent with the strong increase in scatter seen in various scaling relations at these lower masses around this epoch. This suggests that jet feedback drives gas out of haloes in a more stochastic manner, thereby creating large scatter in L_X. Since jet feedback becomes strong at f_{Edd} below a few per cent, which tends to occur when the BH mass grows to above $\gtrsim 10^8 M_\odot$ Thomas et al. (2019), this then connects the larger BHs with the lower f_{gas} and hence lower L_X. We can see this more clearly by examining the L_X and T_X relations more directly using our feedback variant runs, which we do next.

4.2 $L_X - M_{500}$

Fig. 11 shows the median L_X as a function of M_{500} at redshifts $z = 3 \rightarrow 0$ (blue to red) in various colours as indicated in the legend. The upper left-hand panel shows a $50\,h^{-1}$Mpc run with full Simba physics, and the other panels show the No-X run (upper right-hand panel), No-Jet (lower left-hand panel), and No-Feedback (lower right-hand panel), as in Fig. 10.

In full-physics Simba, we see a steady decrease in the lowest luminosities, with the highest luminosities remaining relatively consistent as masses increase from 10^{13} to $>10^{14} M_\odot$. This is inline with what we saw in the $100h^{-1}$Mpc box. We see very little difference in the overall evolution of the No-X run, suggesting that X-ray feedback has minimal effect on the evolution of the X-ray luminosity.
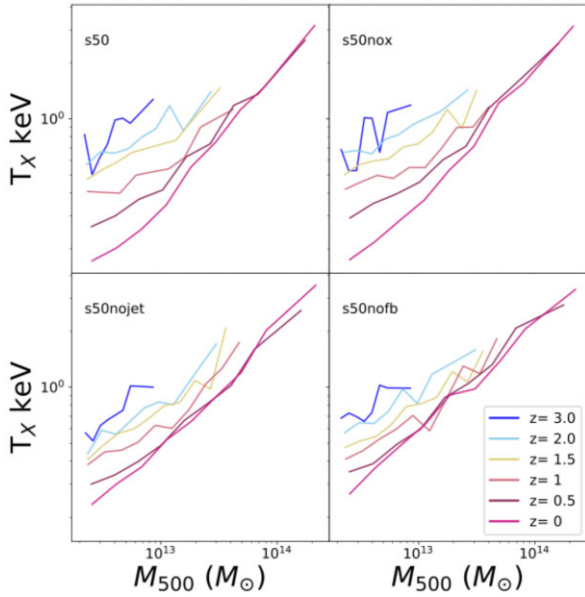
Figure 12. Evolution from $z = 3$ to 0 of the running median of the $T_X - M_{500}$ scaling relation for SIMBA, SIMBA without X-ray feedback, SIMBA without jet feedback, and SIMBA with no feedback. Both SIMBA and No-X show similar evolutions while No-Jet, No-AGN, and No-Feedback show much tighter evolutions indicating jet feedback effect in lower T_X in low mass haloes. No noticeable difference is seen in the scaling relations of the most massive haloes.

Figure 13. Evolution from $z = 3$ to 0 of the running median of the $T_X - L_X$ scaling relation for SIMBA, SIMBA without X-ray feedback, SIMBAwithout jet feedback, and SIMBA with no feedback. Little difference is seen in the NoFB, No-AGN, and No-Jet runs. The No-X run shows an further evolution into the low $T_X - L_X$ region of the plot indicating jets impact on both lower temperatures and luminosities. The SIMBA run shows even further evolution into the lower temperatures indicating that X-ray feedback may have a small effect in these low-temperature haloes at late times.

In contrast, in the No-Jet run we immediately see the impact of jet feedback. Scaling relations at high redshifts match closely with SIMBA's, but much less evolution in L_X is seen, with minimum values not going below 10^{41} erg s^{-1}. The slope of the relation is mostly invariant. NoFB shows a similarly low amount of evolution, showing that SF feedback (and radiative AGN feedback) have fairly minimal impact on this scaling relation. However, there are some non-trivial differences, particularly in the most massive haloes that seem to have lower L_X without any feedback. Hence stellar and radiative AGN feedback seem to work to increase the X-ray luminosities. The origin is likely from the slight increase in hot gas content from NoFB→No-Jet as seen in Fig. 10, because the NoFB case locks more of the halo's baryons into stars (Appleby et al. 2021).

4.3 $T_X - M_{500}$

Fig. 12 shows the median T_X as a function of M_{500} at redshifts $z = 3$ → 0 (blue to red) in various colours as indicated in the legend. The panels are ordered among the feedback variants as before.

We see quantitatively similar behaviour as in the $L_X - M_{500}$ relation, though less dramatically. Jet feedback has the clearest impact on this scaling relation, particularly on the least massive haloes. This can be seen from the difference between the No-Jet in the lower left, and No-X in the upper right. The noticeable difference in the evolution between these two runs begins at $z \sim 1.5$. The outcome of jets is to, perhaps counterintuitively, lower the temperature of the hot gas in low-mass haloes; we speculated this earlier, but here it is clearly demonstrated. At high masses, none of the feedback models have a significant effect on T_X. None the less, it is worth noting that stellar feedback impacts the temperature of low mass at early times, producing a steeper scaling relation. Thus, $T_X - M_{500}$ evolution owes to a combination of different feedback processes operating at different times.
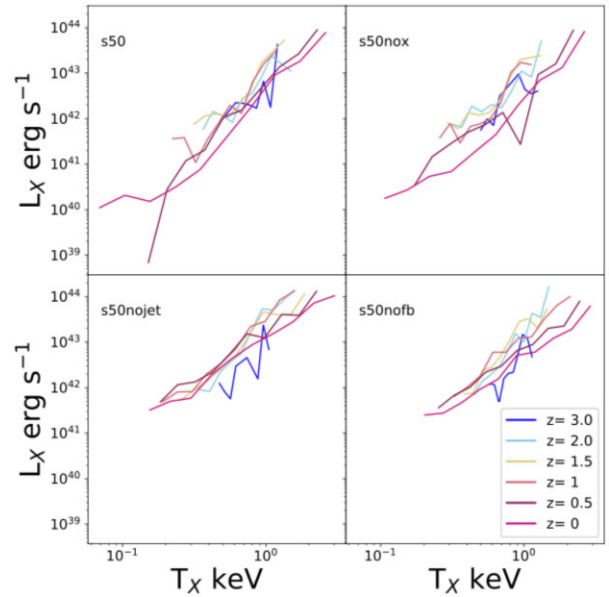
4.4 $L_X - T_X$

Fig. 13 shows the median T_X as a function of M_{500} at redshifts $z = 3$ → 0 (blue to red) in our various feedback runs.

Remarkably, despite clear evolution in $L_X - M_{500}$ and $T_X - M_{500}$, the $L_X - T_X$ relation seems to show little evolution, and indeed not much sensitivity to feedback. This occurs because jet feedback lowers both L_X and T_X, resulting in haloes moving further down the $L_X - T_X$ relation, but not changing its slope or amplitude much. The net effect is that AGN jet feedback 'stretches out' the $L_X - T_X$ relation, but does not substantially alter it. In detail, the $L_X - T_X$ relation does get a bit steeper once jets are turned on, because the drop in L_X due to the evacuation of haloes is more severe than the lowered T_X owing to the hot gas being unbound from low-mass haloes. Hence, AGN jets do break the self-similarity in $L_X - T_X$ at low masses, but the effect is not as dramatic as seen in the individual relations versus M_{500}.

In Robson & Davé (2020), we proposed that SIMBA's scaling relations at $z = 0$ were a result of the implemented jet feedback evacuating hot gas in lower mass haloes. In Figs 11 and 12, SIMBA and No-X show a clear deviation in their evolution after $z = 1.5$, around the time jet feedback kicks in the SIMBA simulations. This lends credence to the idea that jets are responsible for SIMBA's ability to match X-ray scaling relations, which is mainly driven by the gas fraction evolution.

4.5 $Z_X - M_{500}$

Fig. 14 compares the $Z_X - M_{500}$ scaling relations of the various feedback runs, in the same format as the previous plots.

In contrast to the other quantities, jet feedback appears not to be the main driver of evolution in Z_X. In NoFB, we see a steady increase in metallicity over time, which disappears in the No-Jet
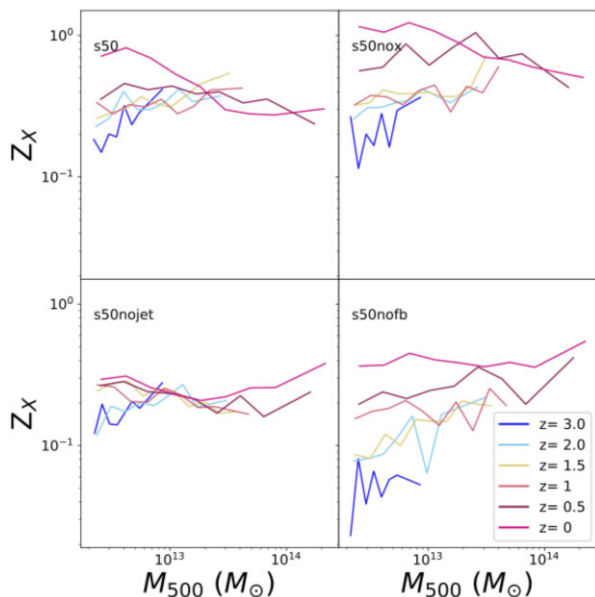
Figure 14. Evolution from $z = 3$ to 0 of the running median of the $Z_X - M_{500}$ scaling relation for Simba, Simba without X-ray feedback, Simbawithout jet feedback, and Simba with no feedback. The no feedback run shows a steady increase in Z_X with decreasing redshift. With the introduction of stellar feedback in the no jet run we see no evolution from $z = 3$ to 0 with stellar winds raising the metallicity to ≈ 0.3 before $z = 3$. The no X-ray run shows jets increasing Z_X at late times, especially amongst small haloes. Finally the full Simba again shows very little evolution, demonstrating X-ray feedback's effect in full quenching haloes in Simba.

case, which instead has metallicities remaining fairly steady $Z_X \approx 0.2-0.3$ solar across time (i.e. roughly the $z = 0$ value in the No-Feedback run). We do not show it, but the No-AGN case is similar to No-Jet. This shows us that stellar feedback is increasing the metallicity of hot gas to observed levels early on and then maintaining them.

None the less the jets do have some effect. In the No-X run, with the introduction of jet feedback we see the X-ray weighted metallicities increase mildly after $z = 1.5$ in the most massive haloes relative to No-Jet, and slightly later but more noticeably after $z = 1$ in the least massive haloes. Hence jets are an important factor for increasing the metallicity in hot intragroup gas at later epochs, presumably by transporting metals out of galaxies in the process of quenching them.

The inclusion of X-ray feedback in the Simba run then sees these late Z_X brought back down to ≈ 0.3 in all but the least massive haloes at $z = 0$. This drop relative to No-X is concordant with the drop in the stellar fraction produced in massive galaxies (Davé et al. 2019), thus indicates the effect of X-ray feedback in fully quenching galaxies in Simba.

Overall, jet feedback has the largest impact in altering the scaling relations from the No-Feedback case. The No-Feedback scalings are, not surprisingly, broadly consistent with self-similar scaling, albeit with deviations at low masses owing to excessive cooling in this model (Davé et al. 2002). Jets evacuate low mass haloes and result in lower temperatures for the gas that remains, giving lower L_X and T_X values. The metallicity, meanwhile, is primarily deposited by star formation feedback at early epochs, though jet feedback tends to result in higher Z_X in low-mass haloes at late epochs.

5 PROFILES

Global $L_X -$ weighted measures tend to weight central regions more heavily where much of the X-ray emission arises, resulting in the properties used in these scaling relations being more sensitive to the core. It is interesting to ask where in radius the various feedback processes in Simba impact the observable properties. To garner a more detailed view of where feedback impacts the halo, we examine the evolution of these haloes' profiles. Thus, we examine the evolution of profiles in the fiducial $100h^{-1}$Mpc Simba run for electron density (n_e), X-ray surface brightness Σ_{L_X}, T_X, and entropy S_X, and subsequently compare with the No-Jet run since we have shown that the jets have the largest impact on the hot gas properties.

We generate projected (2D) profiles for haloes with $10^{12.5} < M_{500} < 10^{13.5}\,\mathrm{M}_\odot$ and $M_{500} > 10^{13.5}\,\mathrm{M}_\odot$, by stacking haloes in these mass bins scaling each to their respective R_{200} values. These profiles are plotted for $z = 2, 1, 0$. Profiles at $z = 3$ show similar trends as at $z = 2$ and so were omitted for clarity.

5.1 Full Simba profiles

Fig. 15 shows the median profiles for electron density (n_e) in the top left-hand plot, L_X surface density ($\Sigma_{L_X} \equiv L_X/A$ where A is the surface area of the 2D radial bin) scaled by its value at R_{200} in the top right-hand panel, T_X scaled by its value at R_{200} in the bottom left-hand panel, and Entropy (S_X) in the bottom right-hand panel. Here, entropy is defined as $T_X/n_e^{2/3}$ and is calculated by dividing the temperature of each particle by its $n_e^{2/3}$ and then calculating the L_X weighted average across the radial bin. Profiles are represented by dotted, dashed, and solid lines for $z = 2, 1$, and 0, respectively. Profiles of haloes with $M_{500} < 10^{13.5}\,\mathrm{M}_\odot$ are blue and haloes with $M_{500} > 10^{13.5}\,\mathrm{M}_\odot$ are red. The shaded areas represent the standard error and are shown on haloes with $M_{500} > 10^{13.5}\,\mathrm{M}_\odot$ at $z = 0$. We scale Σ_{L_X} and T_X by their values at R_{200} in order to highlight the evolution in the shapes of these profiles; the amplitude evolution for these quantities was quantified in the previous section.

The top left-hand panel shows the electron density profiles. The most visible trend in both mass bins is a steady decrease in the amplitude with time. Less evident but still clear is a slight flattening, indicating a stronger decrease in core density. At $z = 2$ and 1 the profiles for $M_{500} < 10^{13.5}\,\mathrm{M}_\odot$ and $M_{500} > 10^{13.5}\,\mathrm{M}_\odot$ lie very close to each other, consistent with self-similarity. However, at $z = 0$, we see that the two mass bins have diverged in amplitude, with more massive haloes having an overall higher electron density. Notably, this occurs at all radii, and is not limited to the core. This is consistent with the stronger removal of hot gas due to jet feedback that heats the gas in lower mass haloes, but is not expected in a scenario where more efficient cooling in lower mass systems depletes the hot gas in the central region.

Moving to the temperature profiles in the lower left panel of Fig. 15, we first note that most of the profiles are within a factor of two of being isothermal (note the small range in y-axis). Within this, however, some notable differences in profile shapes are seen. Even at early epochs, high-mass haloes have a steeper profile than low-mass ones. Both mass bins have steeper profiles with time, and by $z = 0$ they exhibit a mildly cooler core at $R \ll 0.1R_{200}$. None of these core drops are so dramatic as to identify these systems as 'cool core' systems, which have T_X profiles dropping well below $T_X(R_{200})$ in the centres. While some individual profiles do this, the mean profile is not a classic cool-core system in either mass bin. The
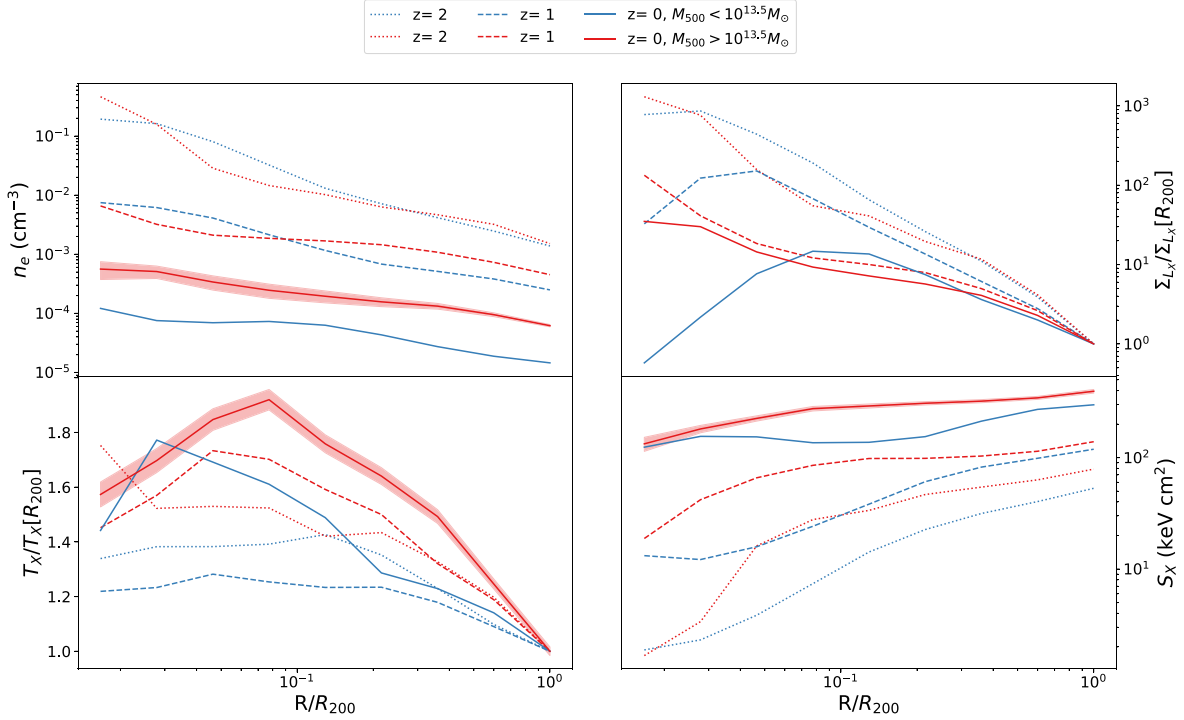
Figure 15. Median Profiles at $z = 2, 1, 0$ for electron density, Σ_{L_X}, T_X, and S_X. $z = 2$ is represented by a dotted line, $z = 1$ by a dashed line, and $z = 0$ by a solid line. The median profiles of haloes with $M_{500} < 10^{13.5}$ $M_\odot$ are coloured blue while those $> 10^{13.5}$ $M_\odot$ are represented by the red lines. The Σ_{L_X} profiles are scaled to their values at R_{200} to accentuate the evolution in shape however the shift in trends can still be seen in the other plots. n_e shows a profile decreasing with radius at all redshifts, with profiles flattening due to a higher decrease in the core regions as we move from $z = 2$ to 0. We also see overall higher densities at all radii within the $M_{500} > 10^{13.5}$ bin at $z = 0$, a shift from the similar levels at the previous redshift. Σ_{L_X} profiles for $M_{500} > 10^{13.5}$ show a slight flattening with redshift. This evolution matches closely in the outer regions of the $M_{500} < 10^{13.5}$ haloes, however, these haloes exhibit a growing low luminosity core, with the radial extent of the core increasing with redshift to $\approx 0.1 R_{200}$ at $z = 0$. T_X profiles show little evolution in shape, however, demonstrate a more significant decrease in overall temperature in the lower mass haloes, bringing both mass bins in line with each other by $z = 0$. S_X profiles flatten with redshift driven by a higher increase in entropy in core regions.

variation among individual profiles and their central cooling times is an interesting study that we leave for future work; here we simply note that there are mild differences in profile shapes in the two mass bins over time.

The electron density plus the temperature are the main determinants of the X-ray luminosity. Fig. 15, top right-hand panel, shows Σ_{L_X} profiles scaled to their value at R_{200}. Overall, the profiles in both mass bins become slightly shallower with time, showing a pronounced central peak at $z = 2$ reflective of the peak in the n_e profile then. Already at $z = 1$, differences emerge in the core, with a slight flattening of the inner profile between $z = 2 \rightarrow 1$ in the low-mass haloes, becoming even more pronounced at $z = 0$. The outer ($R \gtrsim 0.2 R_{200}$) profiles remain fairly consistent at all redshifts, indicating that the drop in X-ray luminosity for low-mass systems at late times (and the associated departures from self-similarity) arises primarily from the core region, likely indicating the effect of jets on the cores of lower mass haloes.

Finally, we investigate the X-ray weighted entropy profiles in the bottom right-hand plot of Fig. 15. Here the combined effect of T_X and n_e can be seen as given by the $S_X \equiv T_X/n_e^{2/3}$ entropy definition. A steady increase in entropy can be seen in both mass bins, with lower mass haloes exhibiting more flattening across redshift. While both mass bins show a similar raising of core entropies, lower mass haloes do appear to exhibit overall lower entropies at early times. This is consistent with the idea that cooling is more effective in low-mass haloes at early epochs, but by $z = 0$, the jet feedback has evacuated

gas such that it raises the entropy particularly strongly in low-mass systems. This raised entropy is likely a critical factor to suppress cooling in these systems in order to keep galaxies quenched.

5.2 No-Jet profiles

We have implicated jets in impacting the evolution of low-mass profiles in comparison with higher mass systems. We can test this more directly by examining the same set of profiles in our No-Jet run. We note that here we must use the $50 h^{-1}$Mpc run here, but we have checked that the profiles in the $50 h^{-1}$Mpc full SIMBA run follows the same trends as those in the $100 h^{-1}$Mpc fiducial volume that we presented in the previous section. However, this does mean that the $M_{500} > 10^{13.5}$ $M_\odot$ bin is notably less populated in the No-Jet case owing to the smaller volume.

Fig. 16 shows the profiles in the No-Jet run, formatted as in Fig. 15, displaying profiles at $z = 0, 1, 2$ (solid, dotted, dashed lines) in high and low halo mass bins (red and blue, respectively).

For the n_e profiles, in the top left-hand plot, we see two interesting effects: First there is significantly less evolution across mass scales, with only an order of magnitude decrease in density, as opposed to the three orders of magnitude decrease seen in Fig. 15. This difference in evolution is most notable in the core regions, with all haloes maintain a much higher core density over redshift, even while the electron density at R_{200} has fairly similar evolution with and without
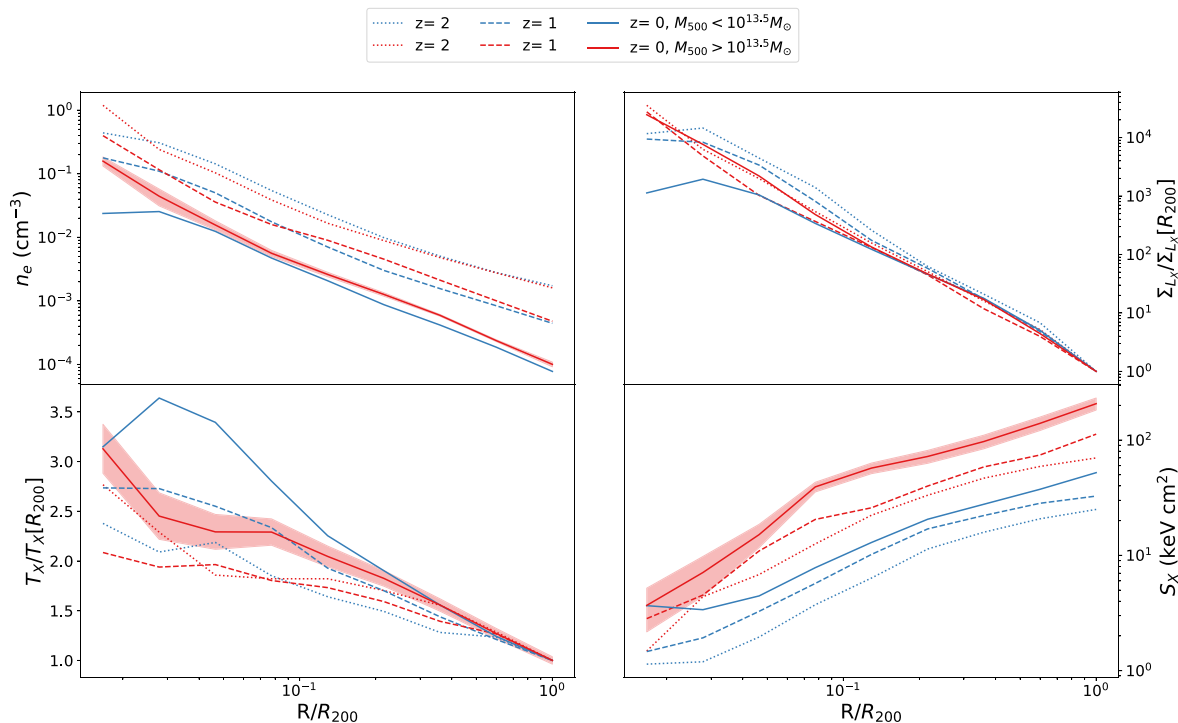
Figure 16. Median profiles at $z = 2, 1, 0$ for electron density, Σ_{L_X}, T_X, and S_X in the $50\,h^{-1}$Mpc No-Jet SIMBA run. $z = 2$ is represented by a dotted line, $z = 1$ by a dashed line, and z = 0 by a solid line. The median profiles of haloes with $M_{500} < 10^{13.5}\,\mathrm{M_\odot}$ are coloured blue while those $> 10^{13.5}\,\mathrm{M_\odot}$ are represented by the red lines. The Σ_{L_X} profiles are scaled to their values at R_{200} to accentuate the evolution in shape however the shift in trends can still be seen in the other plots. n_e profiles experience an overall decrease with redshift, maintaining much steeper profiles than the fiducial runs. There is little difference between mass bins. Σ_{L_X} profiles experience very little evolution in shape, with the least massive haloes developing a slightly flattened core at $z = 0$. T_X profiles experience an overall decrease in both mass bins, however, fail to converge at $z = 0$. Little evolution is seen in the shape of the profiles at either mass bin. S_X profiles experience a smaller increase especially at lower masses, with very little evolution seen in the shape of the profiles.

jets; the electron density profiles without jets are thus much steeper than with jets.

Secondly the two mass bins evolve in line with each other, with the only difference being a flatter inner core electron density seen in the lower mass haloes. Thus without jets, the profiles are much more in line with self-similarity, with perhaps a mild effect from other feedback processes concentrated at $\lesssim 0.03 R_{200}$ in lower mass groups. Comparing with Fig. 15, this implicates jets in lowering the electron densities across the entire mass range, and doing so across all radii.

The T_X profiles in the lower left panel of Fig. 16 also experience a similarly mild evolution. The shapes of the profiles remain fairly constant in both mass bins, with haloes maintaining higher temperature cores. In detail, the T_X profiles are actually steeper for low-mass haloes versus high-mass ones, which is opposite to the trend seen in the full-physics SIMBA case. By $z = 0$, the inner profiles in the low-mass groups show a significant elevation, possibly due to enhanced energy input from other feedback processes combined with cooling out of the lower temperature gas to form into stars. Comparing to Fig. 15, the No-Jet profiles are clearly much steeper, and the effect of jets here is already evident at $z = 2$ with steeper T_X profiles. This may indicate that even early low-level jet feedback works to push hot X-ray-emitting gas from cores to the outer regions. This trend strengthens down to $z = 0$, particularly in the low-mass groups.

In the top right-hand plot of Fig. 16, the Σ_{L_X} profiles are again notable for showing very little evolution in the shape of the profiles,

except for a slightly lower core luminosity seen in the lower mass haloes. This directly mimics the trend seen in the electron densities. Moreover, by $z = 0$, the Σ_{L_X} profiles are definitely steeper than in the fiducial run in Fig. 15. This most clearly demonstrates that it is AGN jet feedback that is primarily responsible for breaking the self-similar scaling of the X-ray emission. Other feedback and cooling effects have a much smaller impact.

Finally, in the bottom right-hand panel of Fig. 16, we show the entropy profiles. We see a steady but slow increase in the normalization of the entropy profiles. The lower mass haloes fail to come in line with the most massive haloes, and most notably neither bin experiences a rise of core entropy with respect to the outer regions. This is in line with the idea that jets work to remove low entropy gas, especially from the cores of haloes. The low central entropy allows for substantial cooling that keeps galaxies fueled and star-forming even in high-mass haloes in the No-Jet run, which does not agree with observations. This highlights how jets are responsible for quenching star formation in massive systems, via their impact on the hot gas in the cores of massive haloes.

Overall we see little to no evolution in the shape of the X-ray profiles in the No-Jet case, along with a smaller evolution in the normalization of these profiles. This indicates that jets not only impact the overall properties, but also importantly how these properties are expressed as a function of radius. Interestingly we see jets having an effect in flattening profiles, or creating larger cores (specifically in the low-mass L_X profiles). Finally, while jets have

a clear impact in the shapes of profiles in both mass bins, larger effects are seen in the normalizations of these profiles in the $M_{500} < 10^{13.5}\,\mathrm{M_\odot}$ bin, highlighting the greater impact of jet feedback on lower mass haloes.

6 SUMMARY

In this paper, we have examined the redshift evolution of the X-ray scaling relations and X-ray profiles of intragroup gas within the SIMBA suite of cosmological hydrodynamical galaxy formation simulations. We consider the scaling relations at particular redshifts from $z = 3 \rightarrow 0$, the median paths of haloes in different mass bins through scaling relation space, and the hot gas and X-ray profiles of intragroup gas. We isolate the physical processes driving this evolution by comparing among feedback variant SIMBA runs with different feedback models turned on an off, in comparison with the baseline model of self-similar evolution. We show that:

(i) SIMBA haloes show are mostly consistent with a self-similar slope of their X-ray scaling relations at $z \gtrsim 1.5$, while at $z \lesssim 1.5$ there are an increasing number of groups that are substantially deviated from self-similarity towards lower halo masses.

(ii) Evolution of the $L_X - M_{500}$ scaling relation sees significant change occurring after $z \lesssim 1.5$ driven primarily by a decrease in L_X among haloes with $M_{500} < 10^{13.5}\,\mathrm{M_\odot}$. This is further corroborated by median tracks of haloes showing that the least massive haloes show a 2 dex drop in L_X for a 0.3 dex increase in M_{500} while the most massive haloes show a slight increase in L_X versus an order of magnitude increase in M_{500} from $z = 3 \rightarrow 0$.

(iii) Evolution of the $T_X - M_{500}$ shows departures from self-similarity towards higher T_X for haloes with $M_{500} < 10^{13.3}\,\mathrm{M_\odot}$, indicating that feedback heating from AGN jets is most impactful in poor groups. Following halo over time indicate that the least massive haloes at $z = 3$ do not lower in T_X suggesting that haloes crossing above $10^{12.3}\mathrm{M_\odot}$ at later epochs are responsible for the lowering of T_X in the smaller haloes.

(iv) The hot gas fraction f_{gas} versus M_{500} shows significant evolution at $z \lesssim 1.5$, with a large drop and increasing in scatter particularly for $M_{500} < 10^{13.5}\,\mathrm{M_\odot}$ systems. This scatter is highly correlated with the BH mass fraction $f_{\mathrm{BH}} \equiv M_{BH}/M_{500}$, such that haloes with central galaxies having high f_{BH} have low f_{gas} and vice versa. Median tracks show that haloes with $M_{500} > 10^{13.5}\,\mathrm{M_\odot}$ have hot gas fractions encompassing the majority of the cosmic baryon fraction, while $M_{500} < 10^{13.5}\,\mathrm{M_\odot}$ haloes show an order of magnitude decrease.

(v) The X-ray weighted metallicity shows a significant trend with the stellar baryon fraction in haloes at early epochs, which gets less pronounced over time. Larger groups have a metallicity around one-third solar, while smaller groups generally have slightly higher metallicity but with a very large scatter.

(vi) The $L_X - T_X$ relation shows an increasing departure from self-similarity with time, with a growing population at $T_X \lesssim 1$ keV having lower L_X that becomes particularly prominent at $z \lesssim 1.5$. The haloes that are most deviant from self-similarity are the ones with the highest f_{BH}, implicating BH feedback as the cause of this deviation.

(vii) To pinpoint the particular physical processes driving the above evolution, we examine smaller $50\,h^{-1}$Mpc SIMBA runs with specific feedback modules turned off. Turning off both AGN and star formation feedback results in little evolution in f_{gas}, and modest evolution in L_X and T_X mostly consistent with self-similarity.

(viii) Introducing stellar (but no AGN) feedback does not change f_{gas}, L_X, or T_X, but it does result in significantly earlier deposition of metals into the hot gas even by $z = 3$.

(ix) Introducing AGN jet feedback has a dramatic impact on scaling relations. Jets are clearly implicated in lowering f_{gas} in $M_{500} < 10^{13.5}\,\mathrm{M_\odot}$ groups, particularly at $z \lesssim 1.5$. This reflects in a dramatic reduction in $L_X - M_{500}$ in such groups over time, and an increased reduction in $T_X - M_{500}$ with time.

(x) Remarkably, the $L_X - T_X$ evolution undergoes a sort of cancellation, in that the lowering of both L_X and T_X results in groups evolving mostly along the relation. The net effect is that groups today end up much more spread out along the $L_X - T_X$ relation, but the overall relation is surprisingly similar in slope and amplitude in all the feedback variants.

(xi) The $Z_X - M_{500}$ evolution is unique in that it is more impacted by stellar feedback than AGN feedback. With no feedback, a steady increase is seen in metallicity. The inclusion of stellar feedback produces hot gas metallicities $>0.1\,Z_\odot$ even by $z = 3$. The inclusion of jet and X-ray feedback then seems to reintroduce a modest level of upwards evolution in metallicity particularly in low-mass haloes, resulting in the final $z = 0$ relation that increases mildly to low halo masses.

(xii) Electron density profiles in SIMBA drop and flatten with time, at all masses. The drop in smaller groups from $z \sim 1 \rightarrow 0$ is however significantly greater than in larger systems. L_X profiles also experience a flattening at all mass ranges, however, it is most prominent at $M_{500} < 10^{13.5}\,\mathrm{M_\odot}$, growing a constant surface brightness core ($R \lesssim 0.1R_{200}$) by $z = 0$. The temperature evolution is not dramatic, but entropy is also flattened, resulting in all groups having median core entropies above 100 keV cm^2.

(xiii) Turning off jet feedback has significant impact on both the shape and normalization of these profiles. Electron density, temperature, and luminosity profiles are steeper. There is much less difference between the two mass bins, with only a very small core appearing at late times in the lower mass groups. The entropy profile is much steeper, with typical entropies at $\sim 0.01R_{200}$ below 10 keV cm^2 at all masses.

These results overall show that the implementation of AGN jet feedback in SIMBA has a significant impact on X-ray properties both globally and in terms of their profiles. It is this feedback that causes strong departures from self-similarity, which tend to become noticeable around $z \sim 1.5$ as AGN jets turn on in central group galaxies, and that results in intragroup gas that closely matches X-ray observations at $z = 0$ as shown in Robson & Davé (2020). The evolution of X-ray profiles provides further constraints on these models, demonstrating the effects of feedback in evacuating low-entropy gas and creating X-ray surface brightness cores particularly in lower mass groups. That AGN jet feedback is the most important driver of X-ray properties in SIMBA is perhaps not very surprising, since SIMBA's AGN feedback was explicitly designed to quench galaxies via energetic input into surrounding gas. Other models could enact the same level of quenching via different mechanisms that could potentially have different impacts on surrounding gas; indeed, EAGLE and IllustrisTNG seem to do exactly this (e.g. Davies et al. 2020). The predictions here are intended to go towards highlighting the connection between galaxy quenching and X-ray properties across a range of redshifts within SIMBA, which provide a baseline for comparison to these other models and eventually forthcoming observations.

We emphasize that our conclusions are based on a single simulation, SIMBA, that was tuned to match galaxy properties. In particular,

the AGN feedback subgrid model was primarily aimed at quenching massive galaxies in accord with various observations. Furthermore, the radiative feedback mode as implemented in Simba may be less effective purely for reasons of numerical overcooling, so it is possible that this mode could be more important than Simba predictions suggest. Our results should thus be viewed towards shaping our understanding of results upcoming X-ray surveys, alongside similar predictions from other models. The intragroup medium provides a testbed for models because most simulations, including Simba, do not explicitly constrain to intragroup gas X-ray properties. Comparisons to observations will thus be critical for determining the viability of and guiding improvements to AGN feedback models, which are at present relatively new and crude within cosmological-scale simulations.

A dearth of observations at these mass scales at $z \gg 0$, along with an overall lack of consensus caused by selection biases in available results, makes it premature to compare the evolution of Simba's groups to X-ray observations. With future missions such as *Lynx* and *Athena* providing significantly deeper observations that will push toward higher redshifts, it should be possible to further constrain these models providing even greater insight into exactly how AGN feedback impacts the growth of groups and clusters. In future work we plan to examine how these next-generation telescopes will help uncover the physics of gas within groups and clusters, with the successes of Simba suggesting that it provides a suitable framework for interpreting these observations.

DATA AVAILABILITY

The raw simulation data and catalogues for all the runs used in this paper are available at https://simba.roe.ac.uk. The X-ray data will be made available on request to the lead author.

REFERENCES

Anglés-Alcázar D., Özel F., Davé R., 2013a, ApJ, 770, 5
Anglés-Alcázar D., Özel F., Davé R., 2013b, ApJ, 770, 5
Anglés-Alcázar D., Davé R., Faucher-Giguère C.-A., Özel F., Hopkins P. F., 2017a, MNRAS, 464, 2840
Anglés-Alcázar D., Faucher-Giguère C.-A., Kereš D., Hopkins P. F., Quataert E., Murray N., 2017b, MNRAS, 470, 4698
Anglés-Alcázar D., Faucher-Giguère C.-A., Quataert E., Hopkins P. F., Feldmann R., Torrey P., Wetzel A., Kereš D., 2017c, MNRAS, 472, L109
Appleby S., Davé R., Sorini D., Storey-Fisher K., Smith B., 2021, MNRAS, 507, 2383
Arnaud M., Pratt G. W., Piffaretti R., Böhringer H., Croston J. H., Pointe-couteau E., 2010, A&A, 517, A92
Barišić I. et al., 2017, ApJ, 847, 72
Barnes D. J., Kay S. T., Henson M. A., McCarthy I. G., Schaye J., Jenkins A., 2017a, MNRAS, 465, 213

Barnes D. J. et al., 2017b, MNRAS, 471, 1088
Best P. N., Heckman T. M., 2012, MNRAS, 421, 1569
Birnboim Y., Dekel A., Neistein E., 2007, MNRAS, 380, 339
Böhringer H. et al., 2007, A&A, 469, 363
Bondi H., Hoyle F., 1944, MNRAS, 104, 273
Borgani S. et al., 2001, ApJ, 561, 13
Borgani S. et al., 2004, MNRAS, 348, 1078
Bower R. G., 1997, MNRAS, 288, 355
Bower R. G., Benson A. J., Malbon R., Helly J. C., Frenk C. S., Baugh C. M., Cole S., Lacey C. G., 2006, MNRAS, 370, 645
Branchesi M., Gioia I. M., Fanti C., Fanti R., 2007, A&A, 472, 739
Christiansen J. F., Davé R., Sorini D., Anglés-Alcázar D., 2019, MNRAS, 499, 2617
Croton D. J. et al., 2006, MNRAS, 365, 11
Cui W., Davé R., Peacock J. A., Anglés-Alcázar D., Yang X., 2021, Nat. Astron., 5, 1069
Davé R., Katz N., Weinberg D. H., 2002, ApJ, 579, 23
Davé R., Thompson R., Hopkins P. F., 2016, MNRAS, 462, 3265
Davé R., Anglés-Alcázar D., Narayanan D., Li Q., Rafieferantsoa M. H., Appleby S., 2019, MNRAS, 486, 2827
Davies J. J., Crain R. A., McCarthy I. G., Oppenheimer B. D., Schaye J., Schaller M., McAlpine S., 2019, MNRAS, 485, 3783
Davies J. J., Crain R. A., Oppenheimer B. D., Schaye J., 2020, MNRAS, 491, 4462
Dubois Y. et al., 2014, MNRAS, 444, 1453
Eisenreich M., Naab T., Choi E., Ostriker J. P., Emsellem E., 2017, MNRAS, 468, 751
Ettori S., Tozzi P., Borgani S., Rosati P., 2004, A&A, 417, 13
Fabian A. C., Allen S. W., Crawford C. S., Johnstone R. M., Morris R. G., Sanders J. S., Schmidt R. W., 2002, MNRAS, 332, L50
Fabian A. C., 2012, ARA&A, 50, 455
Feng Y., Di-Matteo T., Croft R. A., Bird S., Battaglia N., Wilkins S., 2016, MNRAS, 455, 2778
Foschini L. et al., 2017, A&A, 603, C1
Genel S. et al., 2014, MNRAS, 445, 175
Haardt F., Madau P., 2012, ApJ, 746, 125
Heckman T. M., Best P. N., 2014, ARA&A, 52, 589
Henden N. A., Puchwein E., Shen S., Sijacki D., 2018, MNRAS, 479, 5385
Henden N. A., Puchwein E., Sijacki D., 2019, MNRAS, 489, 2439
Hirschmann M., Dolag K., Saro A., Bachmann L., Borgani S., Burkert A., 2014, MNRAS, 442, 2304
Holden B. P., Stanford S. A., Squires G. K., Rosati P., Tozzi P., Eisenhardt P., Spinrad H., 2002, AJ, 124, 33
Hopkins P. F., 2015, MNRAS, 450, 53
Hopkins P. F., Quataert E., 2011, MNRAS, 415, 1027
Kaiser N., 1986, MNRAS, 222, 323
Kaviraj S. et al., 2017, MNRAS, 467, 4739
Khandai N., Di Matteo T., Croft R., Wilkins S., Feng Y., Tucker E., DeGraf C., Liu M.-S., 2015, MNRAS, 450, 1349
Kravtsov A. V., Yepes G., 2000, MNRAS, 318, 227
Krumholz M. R., Gnedin N. Y., 2011, ApJ, 729, 36
Le Brun A. M. C., McCarthy I. G., Schaye J., Ponman T. J., 2014, MNRAS, 441, 1270
Maughan B. J., Jones L. R., Ebeling H., Scharf C., 2006, MNRAS, 365, 509
McCarthy I. G., Schaye J., Bird S., Le Brun A. M. C., 2017, MNRAS, 465, 2936
McNamara B. R., Nulsen P. E. J., 2007, ARA&A, 45, 117
Merloni A., Heinz S., di Matteo T., 2003, MNRAS, 345, 1057
Narayan R., Medvedev M. V., 2001, ApJ, 562, L129
Oppenheimer B. D., Davé R., Katz N., Kollmeier J. A., Weinberg D. H., 2012, MNRAS, 420, 829
Oppenheimer B. D., Babul A., Bahé Y., Butsky I. S., McCarthy I. G., 2021, Universe, 7, 209
Perna M., Lanzuisi G., Brusa M., Cresci G., Mignoli M., 2017, A&A, 606, A96
Pike S. R., Kay S. T., Newton R. D. A., Thomas P. A., Jenkins A., 2014, MNRAS, 445, 1774
Pillepich A. et al., 2018, MNRAS, 473, 4077

Planck Collaboration XIII, 2016, A&A, 594, A13

Planelles S., Borgani S., Fabjan D., Killedar M., Murante G., Granato G. L., Ragone-Figueroa C., Dolag K., 2014, MNRAS, 438, 195

Pratt G. W., Croston J. H., Arnaud M., Böhringer H., 2009, A&A, 498, 361

Reichert A., Böhringer H., Fassbender R., Mühlegger M., 2011, A&A, 535, A4

Robson D., Davé R., 2020, MNRAS, 498, 3061

Röttgers B., Naab T., Cernetic M., Davé R., Kauffmann G., Borthakur S., Foidl H., 2020, MNRAS, 496, 152

Sasaki S., 2001, Publ. Astron. Soc. Japan, 53, 53

Schaye J., Dalla Vecchia C., 2008, MNRAS, 383, 1210

Schaye J. et al., 2015, MNRAS, 446, 521

Somerville R. S., Hopkins P. F., Cox T. J., Robertson B. E., Hernquist L., 2008, MNRAS, 391, 481

Springel V. et al., 2018, MNRAS, 475, 676

Stevans M. L. et al., 2021, ApJ, 921, 58

Sturm E. et al., 2011, ApJ, 733, L16

Thomas N., Davé R., Anglés-Alcázar D., Jarvis M., 2019, MNRAS, 487, 5764

Thompson R., Davé R., Nagamine K., 2015, MNRAS, 452, 3030

Tremmel M., Karcher M., Governato F., Volonteri M., Quinn T. R., Pontzen A., Anderson L., Bellovary J., 2017, MNRAS, 470, 1121

Vikhlinin A., van Speybroeck L., Markevitch M., Forman W. R., Grego L., 2002, ApJ, 578, L107

Vikhlinin A. et al., 2009, ApJ, 692, 1033

Vogelsberger M. et al., 2014, MNRAS, 444, 1518

Volonteri M., Dubois Y., Pichon C., Devriendt J., 2016, MNRAS, 460, 2979

This paper has been typeset from a TeX/LaTeX file prepared by the author.